Large-eddy simulation of a non-equilibrium turbulent boundary layer

Praveen Kumar[1] and **Krishnan Mahesh**[2]

[1]Aerospace Engineering & Mechanics, University of Minnesota, Minneapolis, MN 55455, USA
[2]Naval Architecture and Marine Engineering, University of Michigan, Ann Arbor, MI 48109, USA
Corresponding author: Krishnan Mahesh, krmahesh@umich.edu

Wall-resolved large-eddy simulation (LES) of a non-equilibrium turbulent boundary layer (TBL) is performed. The simulations are based on the experiments of Volino (2020*a J. Fluid Mech.* **897**, A2), who reported profile measurements at several streamwise stations in a spatially developing zero pressure gradient TBL evolving through a region of favourable pressure gradient (FPG), a zero pressure gradient recovery and subsequently an adverse pressure gradient (APG) region. The pressure gradient quantified by the acceleration parameter K was held constant in each of these three regions. Here, $K = -(\nu/\rho U_e^3)\mathrm{d}P_e/\mathrm{d}x$, where ν is the kinematic viscosity, ρ is density, U_e is the free stream velocity and $\mathrm{d}P_e/\mathrm{d}x$ is the streamwise pressure gradient at the edge (denoted by the subscript 'e') of the TBL. The simulation set-up is carefully designed to mimic the experimental conditions while keeping the computational cost tractable. The computational grid appropriately resolves the increasingly thinning and thickening of the TBL in the FPG and APG regions, respectively. The results are thoroughly compared with the available experimental data at several stations in the domain, showing good agreement. The results show that the computational set-up accurately reproduces the experimental conditions and the results demonstrate the accuracy of LES in predicting the complex flow field of the non-equilibrium TBL. The scaling laws and models proposed in the literature are evaluated and the response of the TBL to non-equilibrium conditions is discussed.

Key words: turbulent boundary layers, turbulence simulation

1. Introduction

Turbulent boundary layers (TBL) have been extensively studied since the seminal work of Prandtl (Prandtl 1904), due to their theoretical and engineering relevance. Mean and second-order statistics of the velocity field in TBL evolving under nominally zero pressure

gradients (ZPG) have been extensively reported in the literature (see reviews by Fernholz & Finley (1996), Klewicki (2010) and Smits, McKeon & Marusic (2011)). However, many flows of practical interest have TBL evolving under pressure gradients, both favourable (FPG) and adverse (APG). The FPG is known to stabilise the boundary layer and can reduce turbulence to the extent of relaminarisation (Narasimha & Sreenivasan 1973; Araya, Castillo & Hussain 2015), whereas APG enhances turbulence and can cause flow separation (Simpson 1989).

Several non-dimensional parameters have been proposed to quantify pressure gradient effects on TBL, based on different length and velocity scales used to normalise the free stream pressure gradient ($\mathrm{d}P_e/\mathrm{d}x$). Some of the popular pressure gradient parameters are the Rotta–Clauser pressure gradient parameter (β), acceleration parameter (K) and inner-scaled pressure-gradient parameter (p_x^+), defined as

$$\beta = \frac{\delta^*}{\rho u_\tau^2} \frac{\mathrm{d}P_e}{\mathrm{d}x}, \tag{1.1}$$

$$K = -\frac{\nu}{\rho U_e^3} \frac{\mathrm{d}P_e}{\mathrm{d}x}, \tag{1.2}$$

$$p_x^+ = \frac{\nu}{\rho u_\tau^3} \frac{\mathrm{d}P_e}{\mathrm{d}x}, \tag{1.3}$$

where ν is the kinematic viscosity, ρ is density, δ^* is the displacement thickness, U_e is the free stream velocity and u_τ is the friction velocity defined as $u_\tau = \sqrt{\tau_w/\rho}$. Note that β and K are related as $\beta = -K Re_{\delta*}(U_e^2/u_\tau^2)$, where $Re_{\delta*}$ is the displacement thickness-based Reynolds number and subscript 'e' denotes the value at the edge of the boundary layer.

There are several past studies on TBL evolving under the influence of pressure gradients, using both experiments (Launder & Jones 1969; Jones & Launder 1972; Skåre & Krogstad 1994; Fernholz & Warnack 1998; Warnack & Fernholz 1998; Castillo & George 2001; Jones, Marusic & Perry 2001; Aubertine & Eaton 2005; Harun *et al.* 2013; Knopp *et al.* 2021; Romero *et al.* 2022) and simulations (Spalart 1986; Skote, Henningson & Henkes 1998; Piomelli, Balaras & Pascarelli 2000; Lee & Sung 2009; Bobke *et al.* 2017; Kitsios *et al.* 2017; Lee 2017; Pozuelo *et al.* 2022), primarily focused on near-equilibrium TBL. Strictly speaking, the boundary layer reaches equilibrium when the mean flow and Reynolds-stress components become independent of the streamwise position, when scaled appropriately with local velocity and length scales (Townsend 1956). However, a less restrictive near-equilibrium condition can be defined when the mean velocity defect is self-similar in the outer region, which is true at high Reynolds number (Re) (Marusic *et al.* 2010). Townsend (1956) and Mellor & Gibson (1966) showed that these near-equilibrium conditions can be obtained when U_e is prescribed by a power law such that $U_e \propto (x - x_0)^m$, where x_0 is a virtual origin and m is the power-law exponent, larger than $-1/3$ in order to obtain near-equilibrium conditions. Any high Re TBL with a constant β (including the ZPG TBL where $\beta = 0$) is a particular case of near-equilibrium TBL, in which the outer region has a self-similar mean velocity defect (Marusic *et al.* 2010). Some numerical studies on pressure gradient TBL (for example, Yuan & Piomelli (2014, 2015) and Wu & Piomelli (2018)) have even included the effect of wall roughness in their simulation set-up. The present literature review is not comprehensive as there are several other past studies which have also looked at TBL undergoing separation and reattachment, relaminarisation, unsteady pressure gradients effects, etc. Devenport

& Lowe (2022) reviewed recent progress in equilibrium and non-equilibrium TBL. Bobke *et al.* (2017) studied history effects in APG TBL using wall-resolved large-eddy simulation (LES). Their simulations of flow over flat plate were designed carefully to induce large region of near-constant β. They also simulated TBL with non-constant β and performed comparative studies to quantify history effects on the evolution of APG TBL. They concluded that β and the friction-based Reynolds number (Re_τ) are insufficient to fully characterise the state of a general pressure gradient TBL. Recently, Pozuelo *et al.* (2022) reported wall-resolved LES results of APG TBL where β was held approximately constant at 1.4 up to a momentum-thickness-based Reynolds number $Re_\theta \approx 8700$. Their simulations are the highest Re reported until date for near-equilibrium APG TBL.

The analysis of non-equilibrium TBL poses many challenges. Several length and velocity scales have been proposed for the inner and outer regions of TBL evolving under pressure gradients. Maciel *et al.* (2018) proposed a consistent framework to analyse APG TBL and identified three parameters to characterise APG TBL. These parameters, namely, the pressure gradient parameter, Reynolds number and the inertial parameter were obtained using scaling analysis of the governing equations. They also discussed how their general parameters relate to commonly used quantities like β and Re_τ and the Zagarola–Smits velocity scale (Zagarola & Smits 1998*a,b*).

Recently, Volino (2020*a*) conducted experiments to study TBL subject to pressure gradients. Their experiments were unique in the sense that an initial equilibrium TBL at ZPG is subjected to FPG, then recovered to ZPG, followed by APG. The desired pressure gradient was applied using a ramp as a top wall, which essentially sets K to a constant value in different regions of the ramp. Here K was held constant and mild enough to avoid relaminarisation or separation. The mean velocity and turbulence statistics along with the integral quantities and wall shear determined from them were documented. In particular, profile measurements were reported at 12 streamwise stations (Station 1–12) in their set-up where Station 1, 6 and 9 were located at the beginning of FPG, ZPG recovery and APG regions, respectively. They performed experiments at eight different physical conditions by setting U_e at the inflow and K in the FPG, APG region using different ramps. Their Case 4, where $U_e = 1\,\mathrm{ms}^{-1}$ at the inflow and $K = 5 \times 10^{-7}$ in the FPG region is taken as the reference for the present work. The Re_θ for this case varies from 1578 at Station 1 to 3846 at Station 6. The present gradient causes the boundary layer to become thin in the FPG region and thick in the APG region. Capturing thin boundary layer in FPG region demands fine grid resolution, and thick boundary layer in APG region requires bigger spanwise domain. This particular case was chosen due to its unique combination of pressure gradient and Re range. The pressure gradient for the case is moderate and its Re_τ ranges from 570–1072 (table 1 of Volino 2020*a*), which is moderately high. Higher pressure gradient and Re_τ will significantly increase the computational cost.

The main goals of the present work are to accurately simulate the reference experiment (Case 4 of Volino 2020*a*) and analyse the results to understand the behaviour of TBL in non-equilibrium conditions. Simulation of such non-equilibrium TBL has several challenges. First of all, the rapid thinning and thickening of the boundary layer thickness requires careful design of the computational grid in order to ensure adequate resolution of the inner layer. The boundary layer becomes very thin in the FPG region, which is the most critical region for the present case as any error in this region can cause large mismatch in rest of the flow field downstream. Second, accurate prediction of turbulent stresses and skin-friction at high Re is demanding. Third, the domain size and boundary conditions should be such that the experimental conditions are closely matched without compromising accuracy.

P. Kumar and K. Mahesh

In this work, wall-resolved LES of non-equilibrium TBL is performed, closely matching the set-up of the reference experiment. The present simulations are the first of its kind where the entire streamwise evolution of the non-equilibrium TBL in the reference experiment is captured. The rest of the paper is organised as follows. The simulation details are described in § 2. Results are described in § 3. The present problem is analysed in § 4 where the scaling behaviour, the modelling implications and the response of TBL to non-equilibrium conditions are discussed. The key findings of the present work are summarised in § 5.

2. Simulation details

2.1. *Numerical algorithm*

In LES, large scales are resolved by the spatially filtered Navier–Stokes equations and the effect of small scales is modelled. The spatially filtered incompressible Navier–Stokes equations are

$$\frac{\partial \overline{u}_i}{\partial t} + \frac{\partial}{\partial x_j}(\overline{u}_i \overline{u}_j) = -\frac{\partial \overline{p}}{\partial x_i} + \nu \frac{\partial^2 \overline{u}_i}{\partial x_j \partial x_j} - \frac{\partial \tau_{ij}}{\partial x_j},$$

$$\frac{\partial \overline{u}_i}{\partial x_i} = 0,$$

(2.1)

where u_i is the velocity, p is the pressure and ν is the kinematic viscosity. The overbar $\overline{(\cdot)}$ denotes spatial filtering and $\tau_{ij} = \overline{u_i u_j} - \overline{u}_i \overline{u}_j$ is the subgrid stress. The subgrid stress is modelled using the dynamic Smagorinsky Model (Germano *et al.* 1991; Lilly 1992). The Lagrangian time scale is dynamically computed based on surrogate correlation of the Germano-identity error (Park & Mahesh 2009). This approach, extended to unstructured grids, has shown good performance for a variety of flows including plane channel flow, circular cylinder and flow past a marine propeller in crashback (Verma & Mahesh 2012).

Equation (2.1) is solved using a numerical method developed by Mahesh, Constantinescu & Moin (2004) for incompressible flows on unstructured grids. The algorithm is derived to be robust without numerical dissipation. It is a finite volume method where the Cartesian velocities and pressure are stored at the centroids of the cells and the face normal velocities are stored independently at the centroids of the faces. A predictor–corrector approach is used. The predicted velocities at the control volume centroids are first obtained and then interpolated to obtain the face normal velocities. The predicted face normal velocity is projected so that the continuity equation in (2.1) is discretely satisfied. This yields a Poisson equation for pressure which is solved iteratively using a multigrid approach. The pressure field is used to update the Cartesian control volume velocities using a least-square formulation. Time advancement is performed using an implicit Crank–Nicolson scheme. The algorithm has been validated for a variety of problems over a range of *Re* including flow over axisymmetric hull (Kumar & Mahesh 2018).

2.2. *Computational domain and boundary conditions*

Figure 1 shows a schematic of the computational domain, which is based on the experimental set-up of Volino (2020*a*). The reference coordinate system is chosen such that the streamwise, wall-normal and spanwise coordinates are x, y and z, respectively, and the origin is located on the bottom wall ($y = 0$ plane) at the inflow plane ($x = 0$ plane). The flow is in the direction of positive x. In the reference experiment, the top wall is
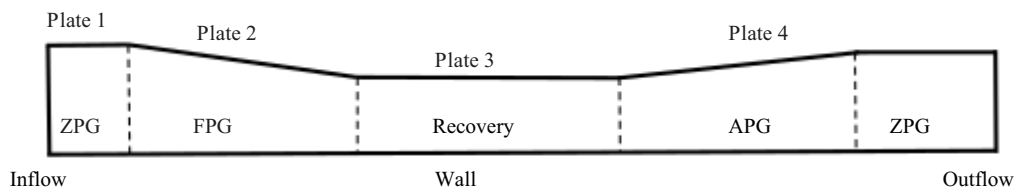
Figure 1. A schematic of the computational domain in xy plane showing ZPG, FPG, recovery and APG regions. Plates 2–4 at the top boundary correspond to those used in the reference experiments (Volino 2020*a*) to impose streamwise varying pressure gradients.

Location	x	Pressure gradient
Plate 1	0–5.46	ZPG
Plate 2	5.46–40.64	FPG
Plate 3	40.64–75.75	ZPG
Plate 4	75.75–102.61	APG
Plate 5	102.61–109.89	ZPG

Table 1. Details of the computational domain in grid units. Note that $\delta = 1$ at the inflow is taken as the reference length for the domain.

comprised of four plates that were adjusted to prescribe a desired K in different regions. In the computational domain, those plates are geometrically identical except for Plate 1 which is made shorter, the reason for that will be discussed later. The test section in the reference experiment ends at the end of Plate 4. However in the computational domain, a horizontal wall (Plate 5) is appended at the end of Plate 4 to ensure minimal effect of the outflow boundary condition.

The boundary layer thickness (δ) and U_e is nominally unity at the inflow plane. The inflow plane ($x = 0$) is located 5.46 units upstream of the beginning of Plate 2. The outflow plane ($x = 109.89$) is 7.28 units downstream of the end of Plate 4. Plates 1 and 5 are parallel to the bottom wall and situated at a wall-normal distance of 7.51 and 7.09 units, respectively, from the bottom wall. Additional details of the computational domain are listed in table 1. The location of the streamwise stations corresponding to the measurement stations in the reference experiment is listed in table 2.

Periodic boundary conditions are applied in the spanwise direction and convective boundary conditions are prescribed at the outflow. Bottom and top boundaries are prescribed as a no-slip condition. A ZPG TBL of desired parameters is prescribed at the inflow plane. This TBL is generated in an auxiliary simulation using the recycle–rescale method of Lund, Wu & Squires (1998) extended to unstructured grids employing the numerical method discussed in § 2.1. The inflow generation method is described and validated for a range of Re_θ in Appendix A.

The bottom wall is tripped far away from the test section in the reference experiment. The use of the auxiliary simulation to generate turbulent inflow enables drastic reduction in the computational cost by reducing the TBL development region in the present set-up while ensuring equilibrium TBL before the start of FPG region. The decision to place the inflow and outflow boundaries as described earlier is based on the prior experience of the authors in simulating spatially developing TBL. Simulations were performed for a domain with a spanwise length of 3 units initially (not shown here). But owing to the rapid growth of TBL thickness in the APG region, the simulations were repeated for a domain with

Station	x
1	2.17
2	10.85
3	17.00
4	22.11
5	28.61
6	37.14
7	51.97
8	63.65
9	71.77
10	80.02
11	84.71
12	89.32

Table 2. Streamwise coordinate of Stations 1–12 where the profiles are compared with the reference experimental data of Volino (2020*a*).

double the spanwise length (6 units) to ensure minimal domain effects. The difference in flow field was minimal between the two domains (see Appendix B).

The grid generation for the present flow problem is challenging due to rapidly varying TBL thickness and strong gradients. The nominally ZPG TBL undergoes a region of FPG, ZPG and APG consequently, which requires a carefully designed non-uniform grid in streamwise and wall-normal directions. The computational grid of the main simulation consists of 395.2×10^6 ($N_x \times N_y \times N_z = 2470 \times 400 \times 400$) hexahedral control volumes. The five segments of the bottom wall shown in figure 1 contain 120, 800, 800, 650 and 100 cells in that order. The authors performed simulations with several coarser grids to arrive at the final grid. The grid is uniform in the z direction only. The first off-wall cell height is 0.0005 throughout the domain at the bottom wall. No attempt was made to resolve the top wall. The first off-wall cell height is ~ 0.1 at the top wall. The grid was generated such that the computational cells are normal to the top wall for at least the first few cells. The grid progressively becomes finer in x going from the inflow to the FPG region, becomes coarser slowly until the beginning of the APG region, after which it maintains uniformity in x direction for the entire APG region. Subsequently, the grid is coarsened slowly towards the outflow plane. Figure 2 shows the grid resolution in viscous units in the domain at the first cell height. The wall-normal and spanwise resolution remains below 0.4 and 12, respectively, throughout the domain. The streamwise grid resolution stays below 36 and 30 in the FPG and APG regions, respectively. The entire grid was partitioned over 5280 processors and the simulations were performed with a time step of 0.001 unit. The flow field statistics were computed for over one flow through time, after the simulations were performed for at least two flow-through times to discard transients.

2.3. *Inflow generation*

An auxiliary LES employing the method described in the Appendix A is performed to obtain a turbulent inflow at $Re_\theta = 1435$ and $\delta \approx 1$. The computational domain of the simulation consists of a box of dimension $100\theta_i \times 30\theta_i \times 60\theta_i$ in the x, y and z directions, respectively, where θ_i is the momentum thickness at the inflow plane. The values of θ_i and Re_{θ_i} are set to 0.1 and 1342, respectively. These values are chosen so that the target plane where $Re_\theta = 1435$ stays sufficiently away from the inflow and outflow boundaries. The grid consists of 300, 200 and 400 cells in the x, y and z directions. The grid is uniform
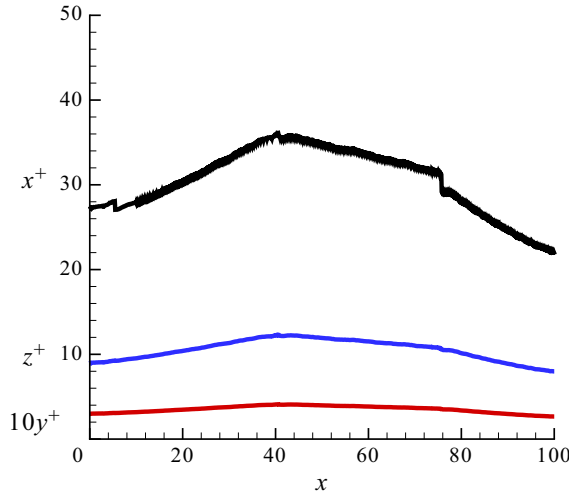
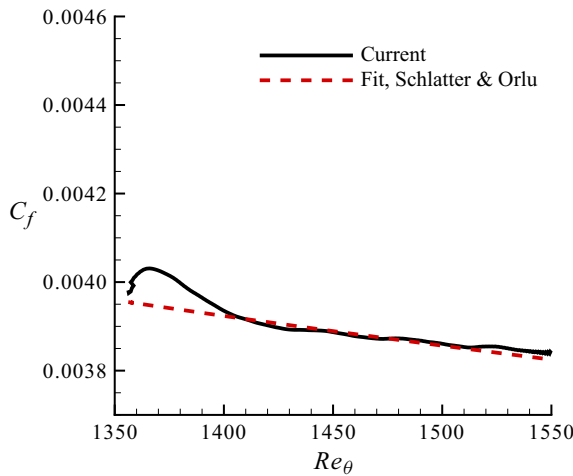Figure 2. Grid resolution in viscous units at the first off-wall cell height.

Figure 3. Here C_f compared with the correlation of Schlatter & Örlü (2010).

in x and z with a clustering in y with 1 % growth to ensure adequate near-wall resolution. Figure 3 shows the comparison of C_f with the correlation of Schlatter & Örlü (2010) showing good agreement away from the inflow. Two profiles are extracted and compared with the direct numerical simulation (DNS) data at $Re_\theta = 1420$ (Schlatter & Örlü 2010), and $Re_\theta = 1551$ (Jiménez *et al.* 2010) in figure 4. Note that throughout this work, $\eta = y/\delta$, where δ is the local boundary layer thickness defined as the wall-normal distance where the mean streamwise velocity reaches 99 % of its local free stream value. The results show very good agreement with the reference data. The grid resolution at these two stations is listed in table 3.

The flow field at the station where $Re_\theta = 1435$ is stored at each time step and interpolated on the inflow plane of the main simulation. Note that the spanwise length of the auxiliary simulation and the computational time step match that of the main simulation.
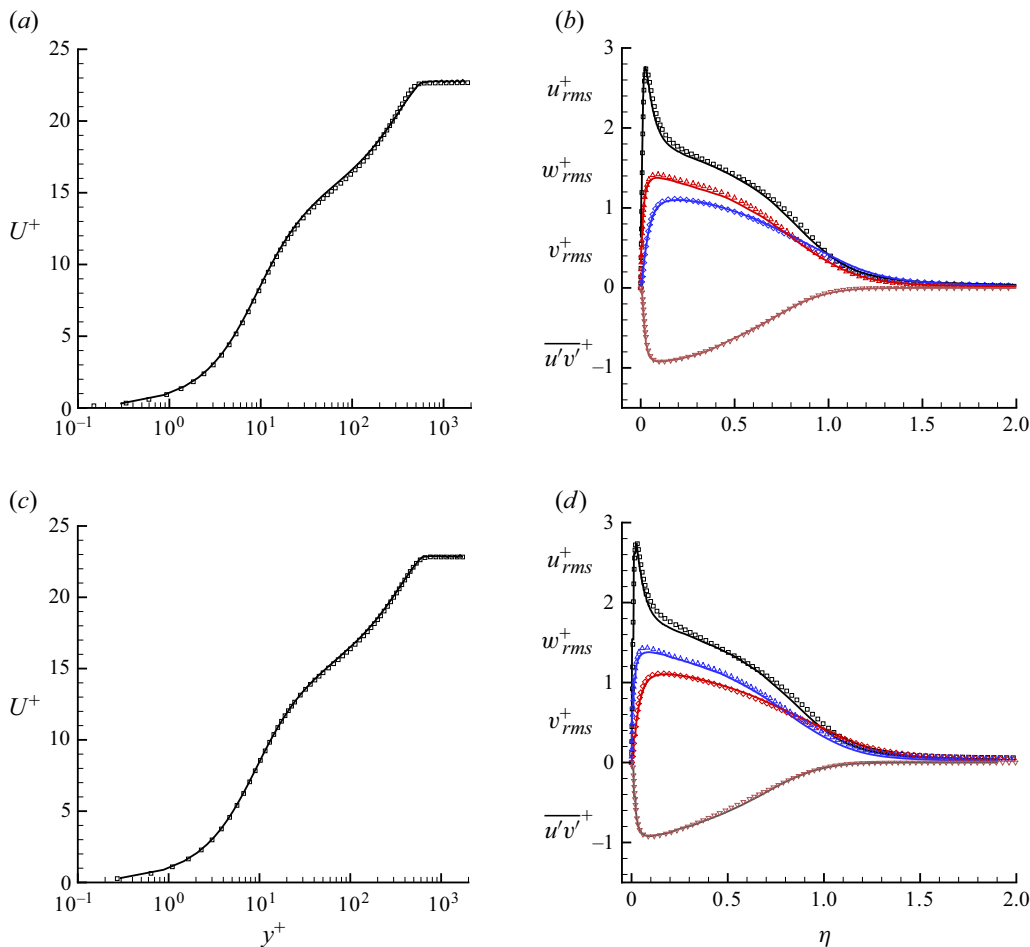
Figure 4. Mean and second-order statistics at $Re_\theta = 1420$ (a, b) and 1551 (c, d). Symbols are DNS from Schlatter & Örlü (2010) (a,b) and Jiménez *et al.* (2010) (c,d).

x	Re_θ	x^+	y^+	z^+
2.55	1420	19.65	0.29	8.84
8.88	1551	19.59	0.29	8.81

Table 3. Grid resolution in wall units at different streamwise stations of the auxiliary simulation.

But the wall-normal extent of the main simulation is larger than that of the auxiliary simulation. So the velocity field is extrapolated to free stream for $y > 30\theta_i$.

As mentioned earlier, the top wall is prescribed a no-slip boundary condition. In the reference experiments, the boundary layer was only tripped at the bottom wall where all the measurements where conducted. Hence, no attempt was made to prescribe a TBL at the top wall in the present set-up. It will be shown later that the present set-up was able to accurately simulate the physical conditions of the reference experiments.
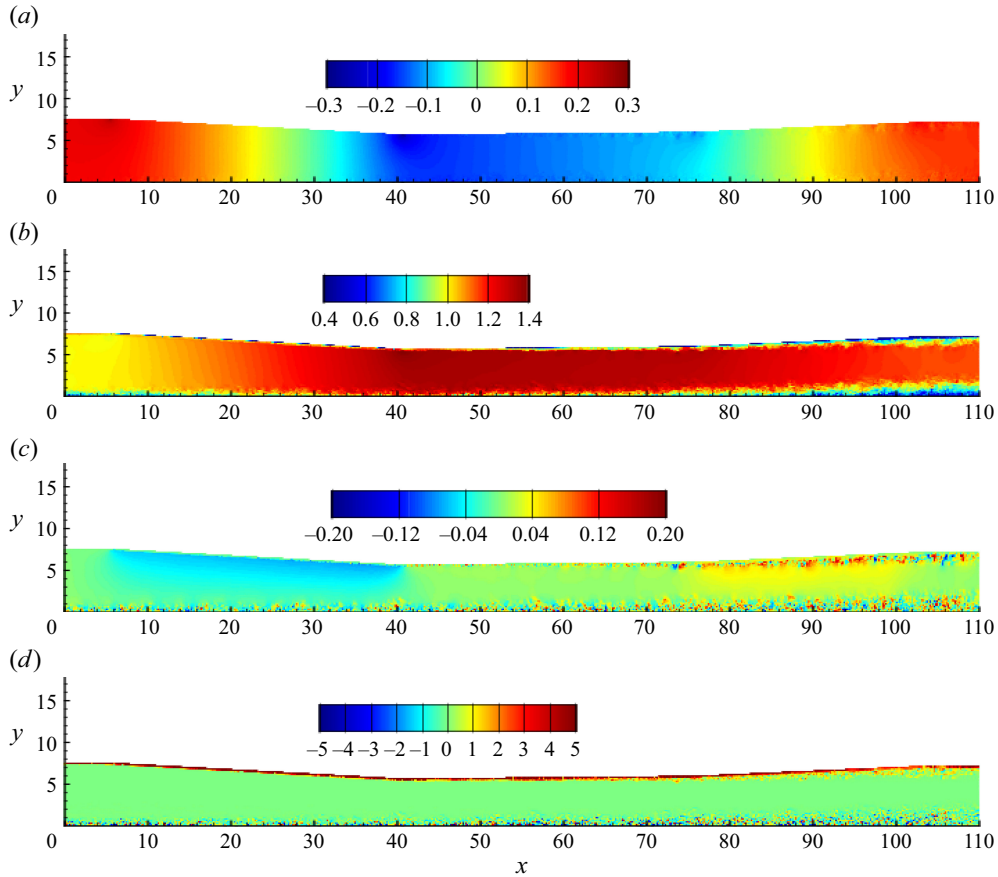
Figure 5. Instantaneous pressure (*a*), streamwise velocity (*b*), wall-normal velocity (*c*) and spanwise vorticity (*d*) in xy plane. The quantities are normalised with the free stream velocity and boundary layer thickness at the inflow plane.

3. Results

3.1. *Instantaneous flow field*

Figure 5 shows contour plots of pressure, streamwise velocity, wall-normal velocity and spanwise vorticity fields in the xy plane. The pressure field shows rapid variation throughout the domain. It first rapidly decreases in the FPG region, followed by nearly constant value in the recovery zone and subsequently, increasing rapidly in the APG region. Such rapid variation in pressure causes rapid change in the thickness of the incoming TBL as it passes through the domain, as evident from the streamwise velocity field (figure 5*b*). The grid is designed to appropriately resolve the TBL of the bottom wall. However, a boundary layer can also be observed on the top wall as well in figure 5(*b*−*d*). Note that the top wall in the reference experiments was intended to prescribe a desired external pressure gradient only and not tripped. Moreover, no attempt was made to characterise the top wall boundary layer. Hence, the simulation set-up did not prescribe any boundary layer on the top wall. However, owing to the no slip condition on the top wall, it is natural to expect it to have a boundary layer development on its own, which ends up growing rapidly and likely turning turbulent in the APG region. At this point, it is not clear how significantly the top wall boundary layer affects the bottom wall TBL. However,
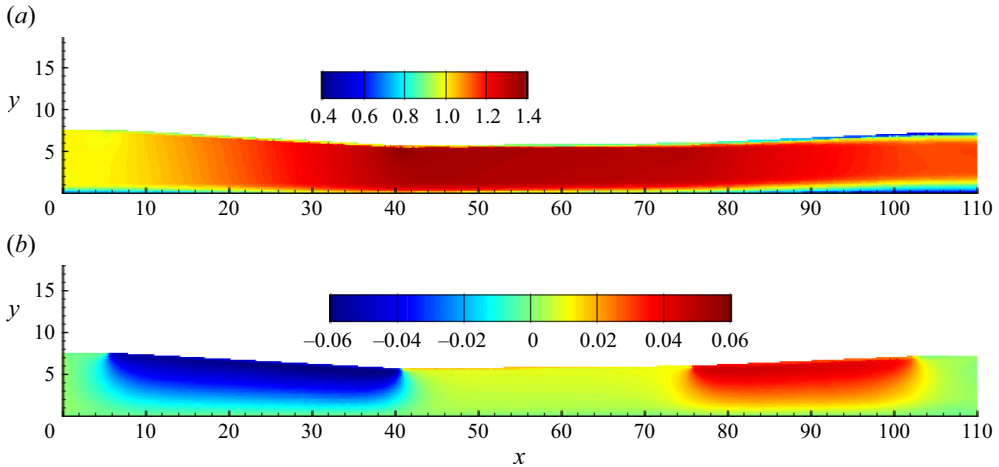
(*a*)

(*b*)

Figure 6. Mean streamwise (*a*) and wall-normal (*b*) velocity fields in xy plane. The quantities are normalised with the free stream velocity and boundary layer thickness at the inflow plane.

it is likely that its effect is negligible in most of the domain. As it will shown later, the results of the TBL at the bottom wall match well with the reference data, confirming that the effect of the top wall boundary layer is minimal. As one would expect, the spanwise vorticity is confined in the boundary layer region of the walls.

3.2. *Mean flow field*

The mean flow field is shown in figure 6 for streamwise and wall-normal components of velocity. The rapidly varying boundary layer thickness is evident on the bottom wall throughout the domain. The top wall has negligible boundary layer thickness until the beginning of APG region. Due to APG, the boundary layer thickness on the top wall grows rapidly and becomes comparable to that of the bottom wall towards the end of the flow domain. The streamwise gradient of U should be equal to the negative of wall-normal gradient of V to satisfy mass continuity. Hence, the region of accelerating free stream shows reduction V away from the wall and *vice versa*. The recovery region on the other hand shows constant V outside TBL as expected from a ZPG region.

3.3. *Comparison with experiments*

The profiles of mean streamwise velocity, resolved root-mean-square (r.m.s.) fluctuations in streamwise and wall-normal velocities along with Reynolds shear stress are compared with the reference data at selected stations (Stations 1, 6, 9 and 12) in figures 7, 8, 9 and 10, respectively. The profile comparisons at other stations are shown in Appendix C for completeness.

The streamwise velocity profiles are shown in the form of velocity defect normalised by the local free stream velocity. The results show very good agreement at all the stations. The grid is able to capture the defect profile adequately even at Station 6, where the boundary layer thickness is very small. The LES results for the r.m.s. of streamwise velocity show some differences at Stations 6–12 in the outer layer. The profiles of the r.m.s. of wall-normal velocity fluctuations and the Reynolds shear stress show good agreement with the reference data at all the stations.

Figure 11 shows the TBL evolution through the flow domain. As observed in figure 11(*a*), (U_e) shows good agreement with the reference data in the FPG region.
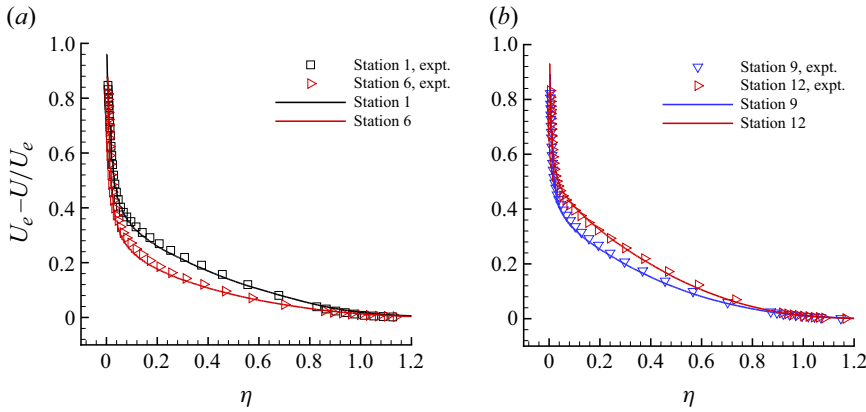
(*a*)

(*b*)

Figure 7. Mean velocity defect profiles (lines) are compared with the reference data (symbols) of Volino (2020*a*) at Stations 1, 6 (*a*) and 9, 12 (*b*).
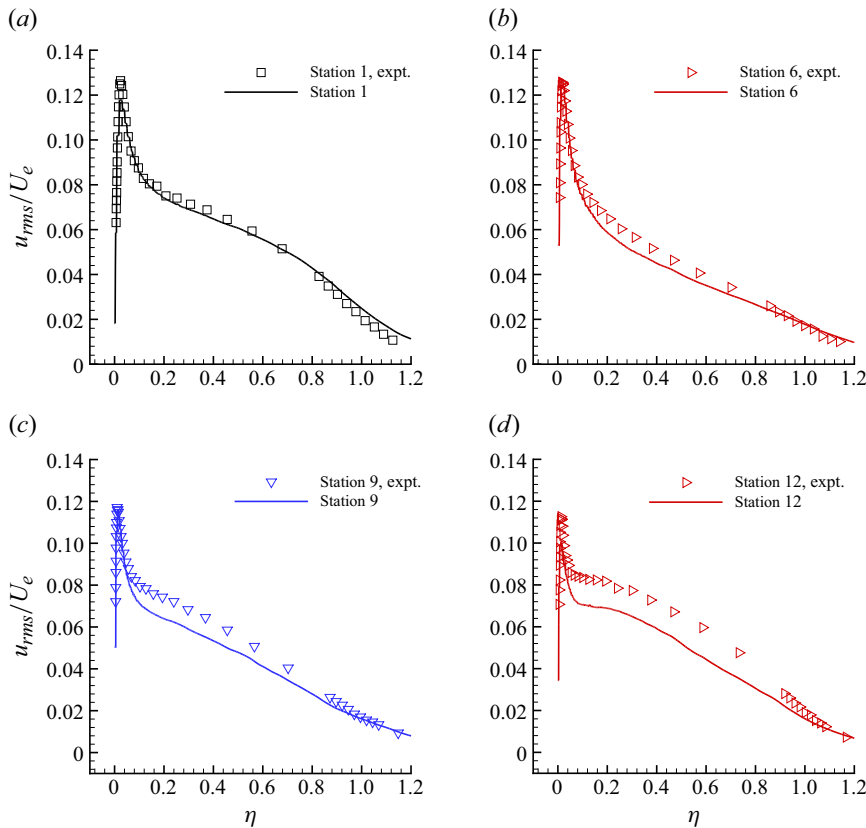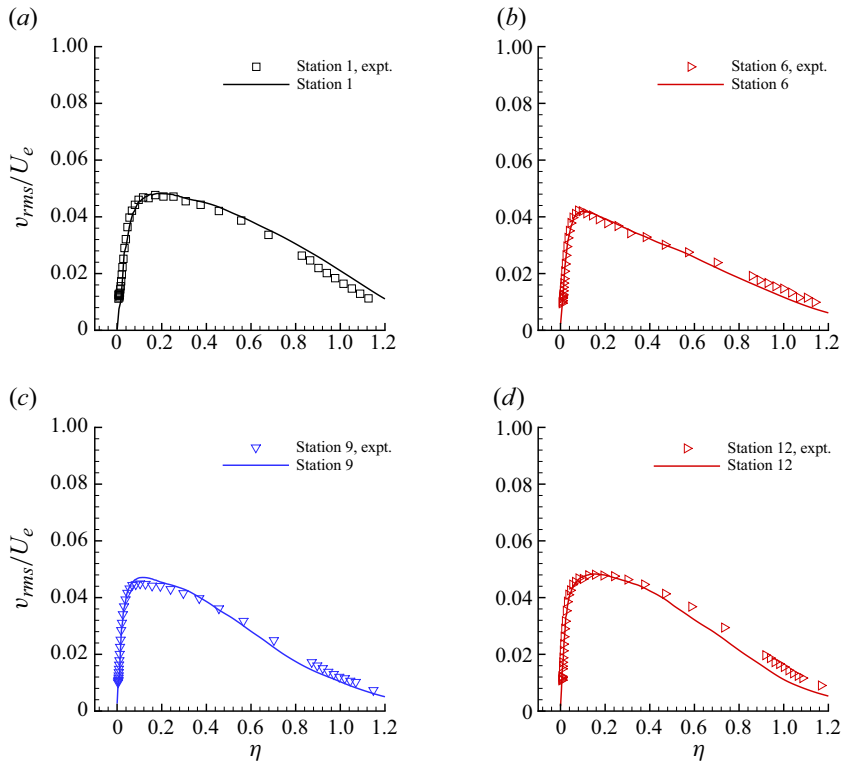
(*a*)

(*b*)

(*c*)

(*d*)

Figure 8. The r.m.s. of streamwise velocity fluctuations (lines) are compared with the reference data (symbols) of Volino (2020*a*) at Stations 1 (*a*), 6 (*b*), 9 (*c*) and 12 (*d*).

There is a slight mismatch in the recovery and APG regions. In particular, the results show slightly lower U_e in the APG region. One possible reason for this behaviour can be the difference in the top wall boundary layer between the LES and the reference experiment. The problem set-up is such that the same mass flow passes through the

Figure 9. The r.m.s. of wall-normal velocity fluctuations (lines) are compared with the reference data (symbols) of Volino (2020a) at Stations 1 (a), 6 (b), 9 (c) and 12 (d).

domain. So if the top wall boundary layer in the present simulation is thinner than the reference experiment, U_e will be smaller at the bottom wall. The LES results indicate that the reference experiment has thicker top wall boundary layer in the APG region than the present simulation. The streamwise evolution of u_τ on the bottom wall is compared with the reference data in figure 11(b). Volino (2020a) obtained u_τ indirectly from the U profile measurements and reported an uncertainty of 3 % which is shown as error bars. The LES results overpredict u_τ in the FPG and recovery regions. The evolution of δ (figure 11c) is captured well throughout the domain except at the last two stations where there is small mismatch. On the other hand, Re_τ (figure 11d) evolution compares well with the reference data throughout the domain. The shape factor (H) is compared with the reference data in figure 11(e), showing good overall agreement. Figure 11(f) shows the evolution of Re_θ. There is a slight underprediction of Re_θ compared with the reference data. This may be reasonable given the comparison of δ and H. Figure 12(a) compares (β) with the reference data. Here $\beta \approx 0$ at the inflow, as expected. The magnitude of β is underpredicted at the first few stations. This observation is consistent with the overprediction in u_τ as shown in figure 11(b). Figure 12(b) shows the streamwise variation in K. Note the value of K in the reference experiment was 5×10^{-7} in the FPG region. Here K appears constant in FPG, recovery and APG regions as expected, and its value is close to the reference experiment in the FPG and recovery regions. However, K is slightly lower in magnitude in the APG region, compared with the experiments where it was set at $K = -5 \times 10^{-7}$. This again can be a consequence of difference in the top wall boundary layer in the present simulation compared with the reference experimental set-up.
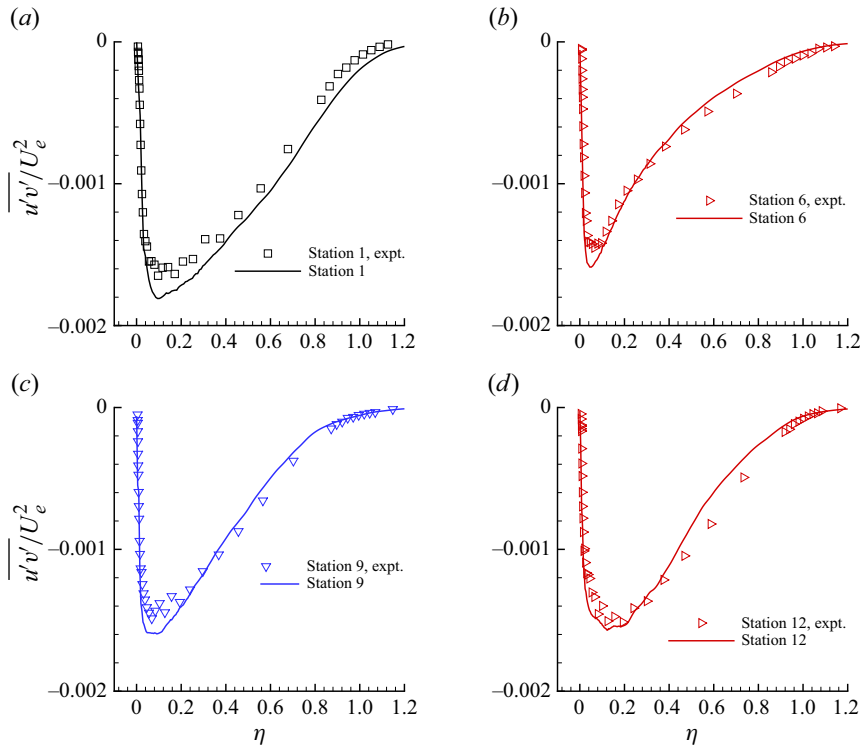
1014 A20-12

Figure 10. Reynolds shear stress profiles (lines) are compared with the reference data (symbols) of Volino (2020*a*) at Stations 1 (*a*), 6 (*b*), 9 (*c*) and 12 (*d*).

Given the complexity of the problem and uncertainty associated with the top-wall boundary layer, the present results for the boundary layer integral quantities can be considered adequate.

4. Analysis

4.1. *Scaling behaviour*

Appropriate length and velocity scales in TBL have been widely studied in the literature. In particular, U_e and δ are often used as appropriate scales to collapse defect profiles in the outer layer of TBL. Volino (2020*a*) showed that defect profiles did not collapse using U_e and δ. In the present section, appropriate length and velocity scales are sought for the present case using the reference data of Volino (2020*a*).

Zagarola & Smits (1998*a*) proposed a velocity scale ($u_{zs} = U_e \delta^*/\delta$, called the ZS scaling henceforth) for pipe flow as an appropriate outer velocity scale, which was able to collapse the outer-layer velocity profiles. The ZS velocity scale was later found to be appropriate even for ZPG TBL (Zagarola & Smits 1998*b*; George 2006). Wei & Maciel (2018) derived u_{zs} from the mean continuity equation in ZPG TBL. Maciel *et al.* (2018) analysed the scaling of APG TBL and concluded that u_{zs} was appropriate velocity scale for a variety of TBL databases they analysed.

Recently, Pirozzoli & Smits (2023) proposed a new set of velocity (u_{ps}) and length (δ_{ps}) scales for outer layer of TBL (called the PS scaling henceforth) given by

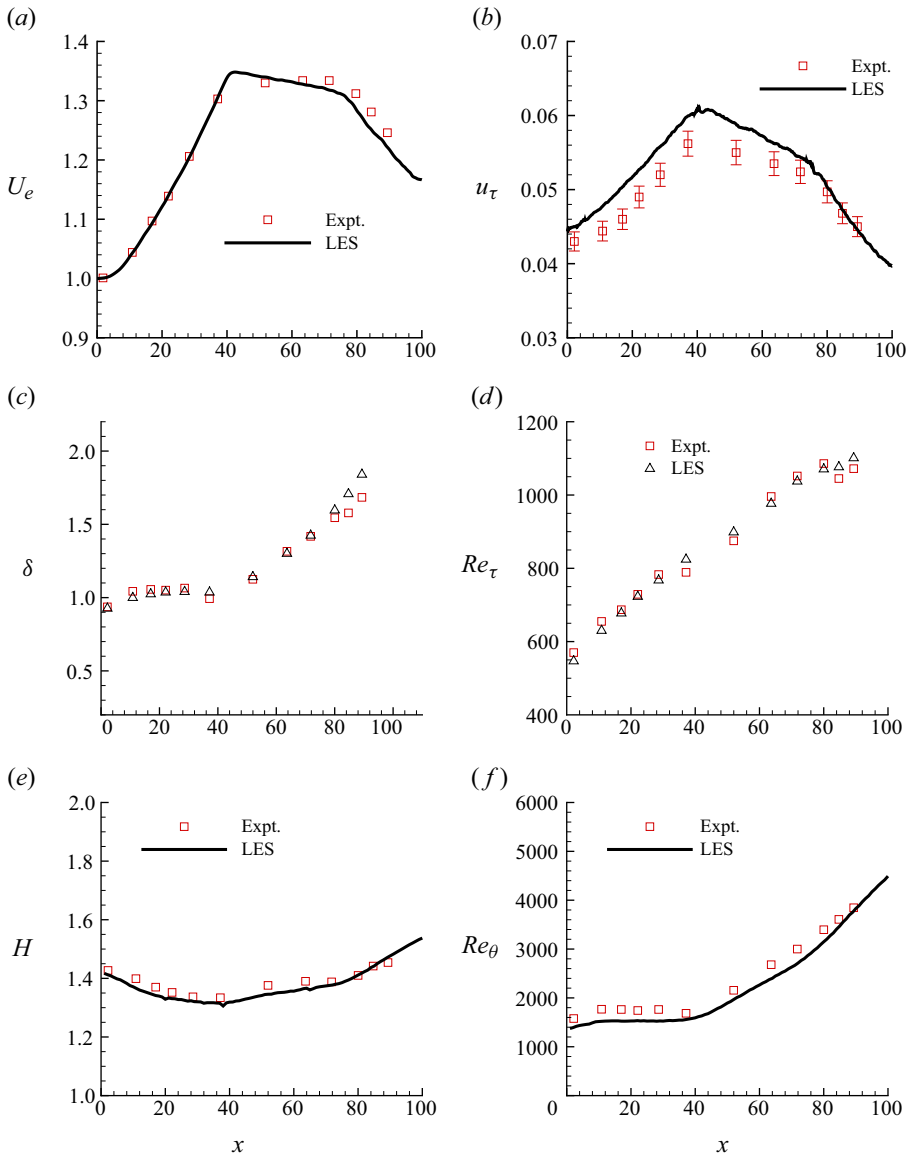$$u_{ps} = \left(\frac{H-1}{H}\right) U_e, \tag{4.1}$$

1014 A20-13

Figure 11. Here U_e, (a), u_τ (b), δ (c), Re_τ (d), H (e) and Re_θ (f) are compared with the reference data. Error bars of 3 % are shown in (b) as reported in Volino (2020a). Here U_e and u_τ are normalised with the free stream velocity at the inflow whereas δ is normalised with the inflow boundary layer thickness.

$$\delta_{ps} = \left(\frac{H}{H-1} \right) \delta^*. \tag{4.2}$$

They tested their scaling on various ZPG TBL databases showing good collapse in the outer layer. It remains unclear if ZS and PS scalings would hold for a non-equilibrium TBL such as the present case.

The applicability of ZS and PS scales is assessed in figure 13 using the reference experimental data. The results show that both these scalings collapse the velocity defect
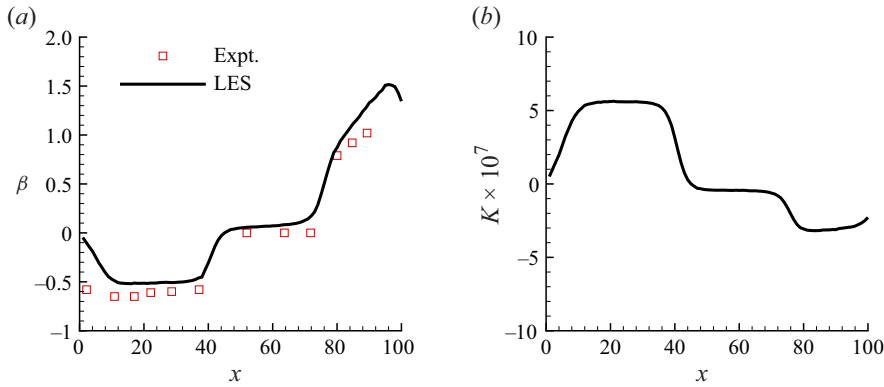
1014 A20-14

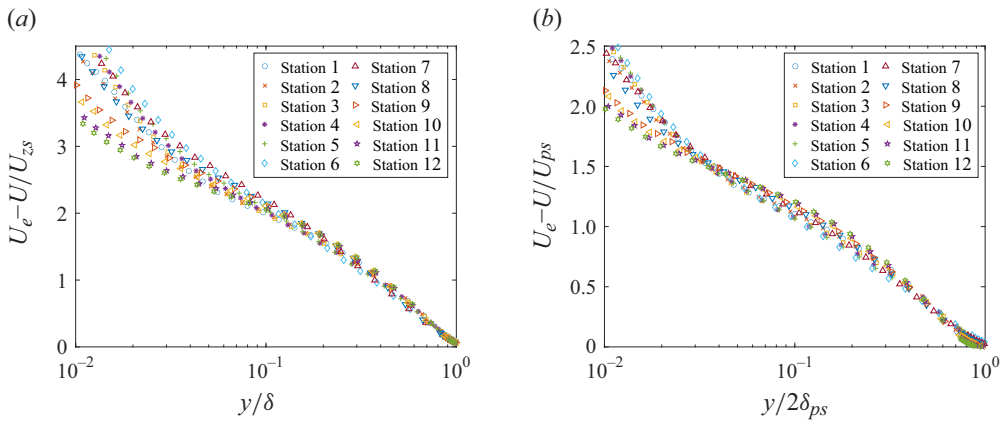Figure 12. The streamwise variation in β (*a*) and K (*b*).

Figure 13. Velocity defect in the scaling proposed by Zagarola & Smits (1998*a*) (*a*) and Pirozzoli & Smits (2023) (*b*) at all the stations.

profiles adequately well in the outer layer, with PS scaling performing slightly better as one moves closer to the wall. The PS scaling is able to collapse the defect profiles in the FPG, ZPG and APG regions adequately, suggesting that even the non-equilibrium effects are adequately captured in u_{ps} and δ_{ps}. Overall, it can be concluded that PS scaling appears to be generally applicable to TBL ranging for equilibrium, near-equilibrium and the present non-equilibrium case. However, its applicability to stronger non-equilibrium cases is yet to be evaluated.

Next, the scaling of u_{rms} is considered. Alfredsson, Segalini & Örlü (2011) proposed a scaling for u_{rms} in the outer layer in the TBL,

$$\frac{u_{rms}}{U} = a + b\frac{U}{U_e}, \tag{4.3}$$

where $a = 0.286$ and $b = -0.255$, which was also found to hold for other wall-bounded flows (Alfredsson, Örlü & Segalini 2012). Figure 14 shows u_{rms}/U profiles plotted against U/U_e for the FPG, ZPG and APG regions. The line in the figures correspond to (4.3) evaluated at Station 2, Station 7 and Station 10 in figures 14(*a*), 14(*b*) and 14(*c*), respectively. The profiles collapse to (4.3) surprisingly well in all three regions. Note that
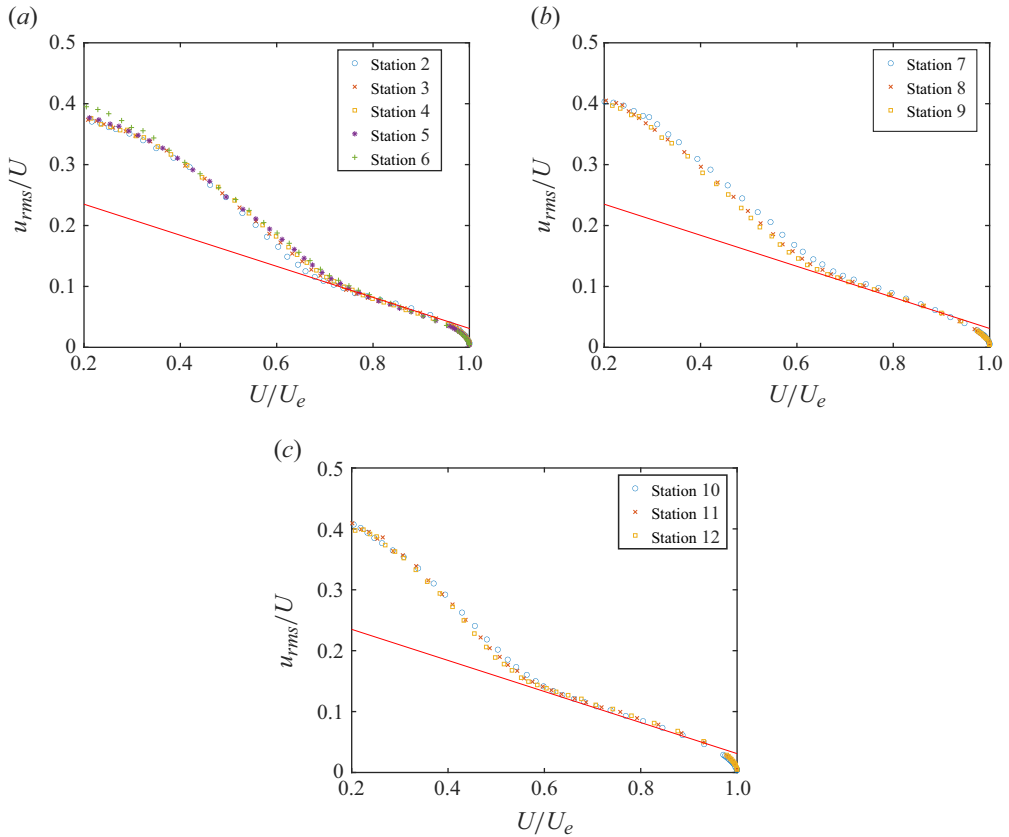
Figure 14. Here u_{rms}/U profiles in FPG (*a*), ZPG (*b*) and APG (*c*) regions along with (4.3) (line) evaluated at Station 2 in (*a*), Station 7 in (*b*) and Station 10 in (*c*).

Stations 2, 7 and 10 are chosen as they are the first station in each of these regions. Choosing a different station to evaluate (4.3) would not make any difference in the results. It is worth mentioning that Dróżdż *et al.* (2015) proposed a modification to (4.3) for pressure gradient TBL by including $\sqrt{H}$ in the denominator of the left-hand side and modifying the values of *a* and *b* for different pressure gradient conditions. It appears that such modifications are not needed for the present case where (4.3) adequately describes the linear region in figure 14.

4.2. *Modelling implications*

Mean total shear stress (T) in the TBL is the sum of viscous and Reynolds shear stress. In the outer layer, the viscous stress is negligible. Hence, $T \approx -\overline{u'v'}$ in the outer layer. Kumar & Mahesh (2021) observed that T^+ plotted against η was insensitive to Re for ZPG TBLs. This observation holds even for APG TBL under near-equilibrium conditions when β is held constant (Kumar & Mahesh 2022). Figure 15 shows $-\overline{u'v'}^+$ plotted against η in the FPG, recovery and APG regions. It is observed that the mean shear stress in the outer layer does not collapse onto a single curve, except in the recovery region where the pressure gradient is negligible and a reasonable collapse is observed for Stations 8 and 9. In the FPG region, $-\overline{u'v'}^+$ keeps decreasing from Station 2–6 for a given η for $\eta > 0.1$. The
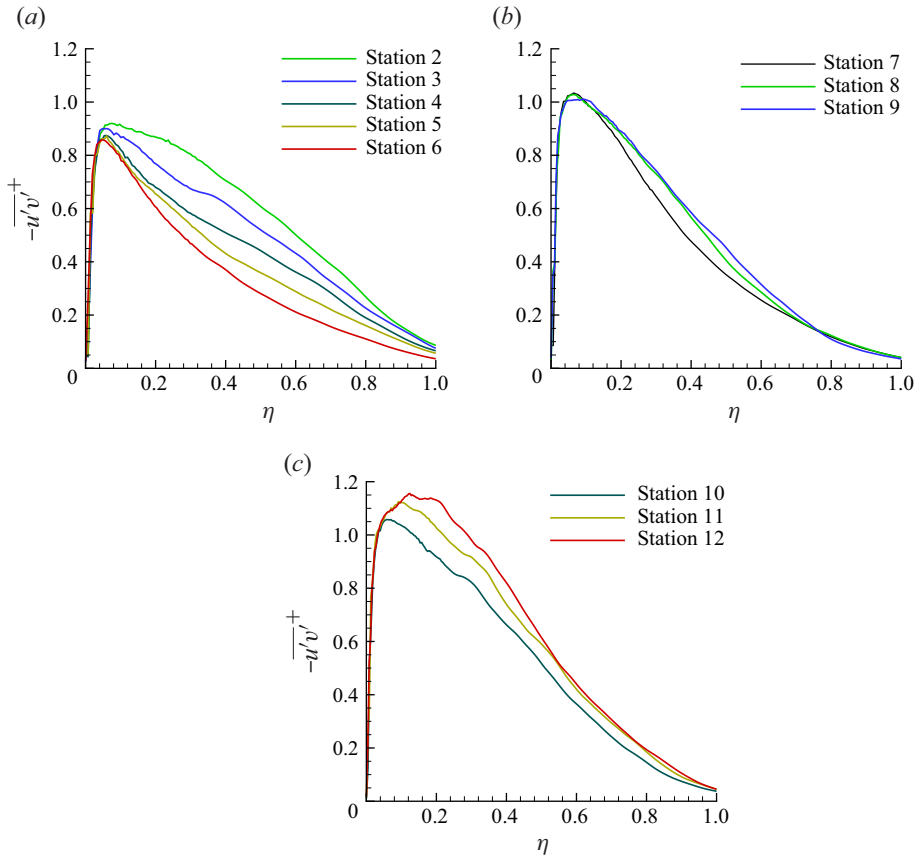
Figure 15. Reynolds shear stress profiles in FPG (*a*), recovery (*b*) and APG (*c*) regions.

trend is opposite in the APG region. Therefore, the total shear stress model of Kumar & Mahesh (2022) derived for near-equilibrium pressure-gradient TBL (i.e. β held constant) is not expected to work for the present case.

Kumar & Mahesh (2021) also proposed a model for wall-normal velocity (V) in ZPG TBL. They observed that V scaled with its edge value collapse well for a range of Re when plotted against η. This led them to fit a hyperbolic tangent function with two constants to obtain a model for V. Later, they extended the model for pressure-gradient TBL by simply multiplying it by a function to enforce it to satisfy the continuity equation outside the boundary layer. Figure 16 shows V/V_e plotted as a function of η for the FPG, recovery and APG regions. First thing to note is that V_e appears to be appropriate scale for V even in non-equilibrium TBL. The collapse is the best in the APG region. It is interesting to observe that the shape of V/V_e is very different than what is observed for equilibrium and near-equilibrium TBL (Kumar & Mahesh 2021, 2022). Even in the recovery region, which is nominally at ZPG conditions, the profile shape of V/V_e deviates significantly from the ZPG TBL profiles shown in Kumar & Mahesh (2021). This behaviour suggests that the V/V_e model of Kumar & Mahesh (2022) which showed good performance for near-equilibrium TBL may not hold in non-equilibrium TBL.

In particular, it appears that $V/V_e \approx \eta$ in FPG and APG regions. This behaviour can be explained using continuity equation as follows. Using the continuity equation for mean
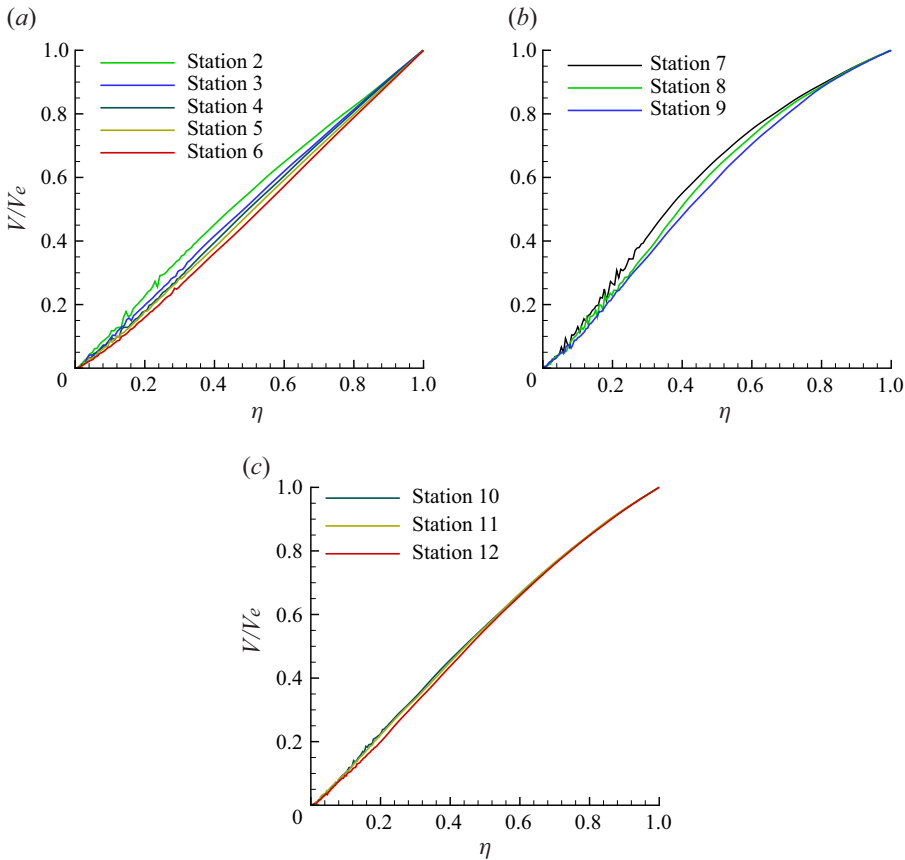
Figure 16. Mean wall-normal velocity profiles in FPG (*a*), recovery (*b*) and APG (*c*) regions.

flow, it can be shown that

$$\frac{\partial V}{\partial y} = -\frac{\partial U}{\partial x} \approx -\frac{\mathrm{d}U_e}{\mathrm{d}x} \implies V = -y\frac{\mathrm{d}U_e}{\mathrm{d}x}. \tag{4.4}$$

It is easy to see that (4.4) will lead to $V/V_e \approx \eta$, as observed in FPG (figure 16*a*) and APG (figure 16*c*) regions.

4.3. *Response of TBL to non-equilibrium conditions*

In the present study, an equilibrium TBL evolves under streamwise varying pressure gradient conditions, from favourable to zero to adverse. In order to understand the response of the TBL to such non-equilibrium conditions, Volino (2020*a*) plotted the difference in velocity defect $(A_{ZPG} - A)$ as a function of streamwise location at $\eta = 0.4$, where $A = (U_e - U)/U_e$. Here A_{ZPG} was obtained from the prior ZPG experiments (Volino 2020*b*). Here, a change function $\Delta(f) = f - f_0$ is defined, where f is a flow quantity and the subscript '*0*' denotes the inflow plane. Here Δ quantifies the change in a flow quantity with respect to the inflow plane as the TBL evolves through the domain.

The Δ of U and turbulent kinetic energy (TKE) in inner units are shown in figure 17 at three constants $\eta = 0.1, 0.2$ and 0.4. Note that for a ZPG TBL, $\eta < 0.2$ is approximately the extent of the inner layer. Therefore, $\eta = 0.1$ and $\eta = 0.4$ location in TBL can be considered
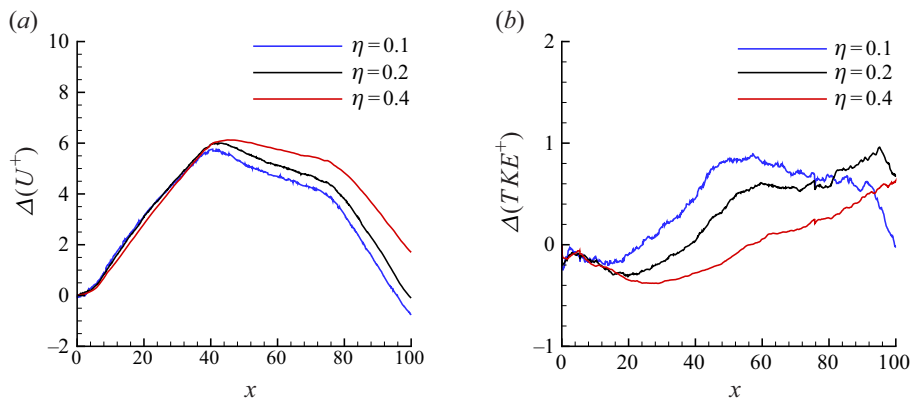
Figure 17. Streamwise evolution of the change in U^+ (a) and TKE^+ (b) at $\eta = 0.1$, 0.2 and 0.4.
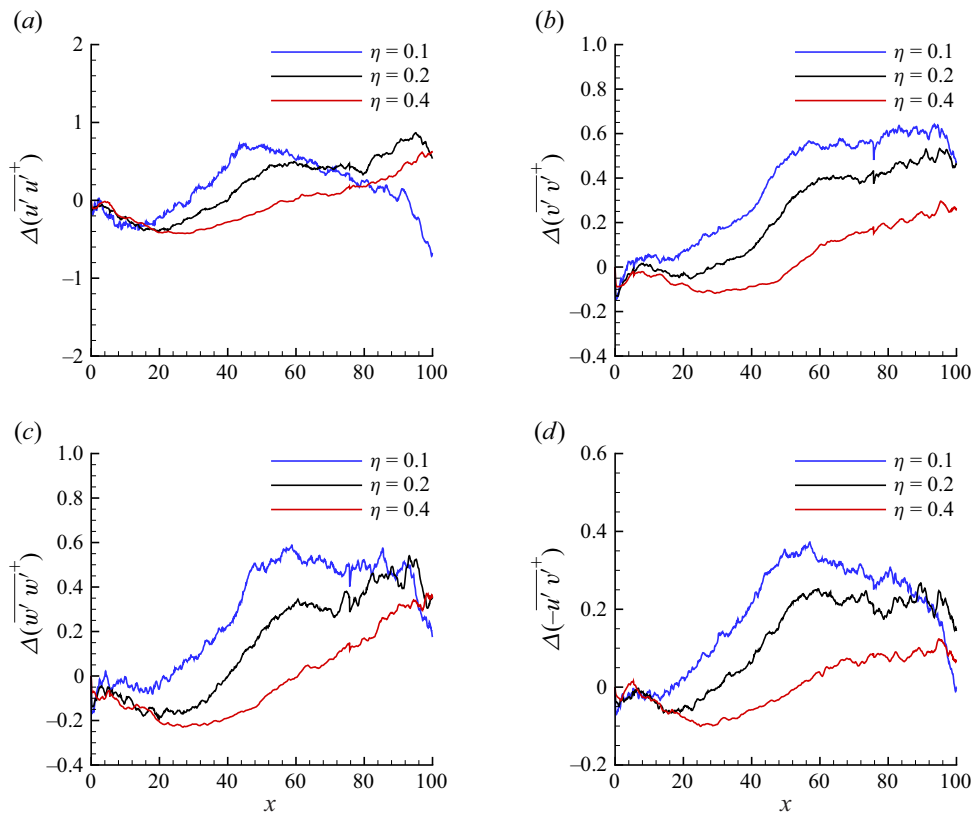

Figure 18. Streamwise evolution of the change in Reynolds stress components: $\overline{u'u'}^+$ (a); $\overline{v'v'}^+$ (b); $\overline{w'w'}^+$ (c); $-\overline{u'v'}^+$ (d) at $\eta = 0.1$, 0.2 and 0.4.

to represent the inner and outer layer, respectively. Recall that the FPG region extends from $x = 5.46$ to 40.64, followed by a recovery region up to $x = 75.75$ and an APG region until $x = 102.61$.

The $\Delta(U^+)$ at the shown η locations appears identical in the FPG region, beyond which the change increases as η increases throughout the rest of the flow domain. The plot suggests that the response of the inner scaled velocity field to the FPG condition is same at all shown η locations. In the subsequent regions, $\Delta(U^+)$ increases with increase in η. The response of TKE (figure 17b) appears similar at all η locations until halfway in the FPG region, beyond which the lowest η location shows the largest value until the end of the recovery region. In the APG region, the Δ in TKE decreases for $\eta = 0.1$, whereas the other η locations show an increase.

In order to better understand the response of TBL, the change in different components of the Reynolds stress tensor are shown in figure 18 at the same η locations as figure 17. The Δ in the streamwise component shows identical decrease in the first-half of the FPG region at all η locations, beyond which all the η locations show increasing trend for rest of the FPG region. In the APG region, the $\eta = 0.1$ location shows a decrease, whereas the other locations maintain an increasing trend. This is consistent with the APG TBL behaviour where the streamwise component increases in the outer layer as the TBL evolves. The Δ in the wall-normal component shows increasing trend throughout the domain, whereas the spanwise component behaves similar to the streamwise component. So the behaviour of TKE where it drops in the latter-half of the APG region at $\eta = 0.1$ appears to be the result of drop in streamwise component. The Reynolds shear stress increases from the middle of the FPG until the middle of the recovery region, followed by a nearly constant value until the mid of the APG region, and subsequent drop in the rest of the APG region.

The Reynolds stress components can be used to define anisotropy tensor as

$$b_{ij} = \frac{\overline{u_i u_j}}{\overline{u_k u_k}} - \frac{\delta_{ij}}{3}, \qquad (4.5)$$

where δ_{ij} is the Kronecker delta. In the limit of one-dimensional turbulence, $b_{11} = 2/3$ and $b_{22} = b_{33} = -1/3$. Figure 19 shows the streamwise variation in b_{11} and b_{22} at three constant η locations. As expected, b_{11} and b_{22} are quite different than the one-dimensional limiting values. The values remain fairly constant beyond the middle of the FPG region for $\eta = 0.2$ and 0.4 locations, suggesting that the anisotropy of the flow does not change in the latter-half of the domain at these locations. The $\eta = 0.1$ location shows the largest variation, where b_{11} decreases while b_{22} increases starting from the recovery region.

5. Summary

Wall-resolved LES of a non-equilibrium smooth wall TBL is performed, closely matching the experimental set-up of Volino (2020a). The computational domain is carefully chosen to match the physical conditions in the reference experiment while keeping the computational cost tractable. The grid is carefully designed to ensure that the streamwise and wall-normal gradients are adequately captured. The detailed comparisons of the flow field with the reference data show that the LES is successful in predicting the non-equilibrium TBL. The simulations reveal the importance of capturing the FPG region accurately, which is the most critical part of the present flow problem. The boundary layer is very thin in the FPG region, requiring careful design of the computational grid.

The scaling analysis reveals that the velocity and length scales proposed by Pirozzoli & Smits (2023) are adequate for the present non-equilibrium TBL case. However, its
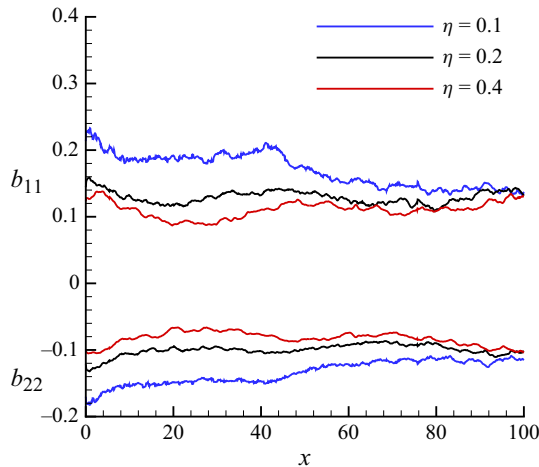
Figure 19. Streamwise evolution of b_{11} (*a*) and b_{22} (*b*) at $\eta = 0.1$, 0.2 and 0.4.

general applicability in stronger non-equilibrium remains to be evaluated. Additionally, the scaling of u_{rms} based on the diagnostic plot (Alfredsson *et al.* 2011) holds well in the outer layer of the present case. The results also show that the V and T models developed in the literature for near-equilibrium TBL require substantial improvements to incorporate the non-equilibrium effects. The response of the flow to non-equilibrium conditions is described at various η locations in terms of the inner scaled mean velocity field and Reynolds stress components as well as the components of the anisotropy tensor.

The present work is the first attempt to perform resolved LES of the reference experimental set-up, to the best of our knowledge. The simulations complement the experiments of Volino (2020*a*) towards the goal of better understanding the behaviour of TBL in non-equilibrium conditions. Future work will focus on leveraging the present data to develop models for mean flow quantities and better wall models to enable such simulations at even higher Re.

Declaration of interests. The authors report no conflict of interest.

Appendix A. Turbulent inflow generation

A.1. *Brief description of the method*

Unlike fully developed channel or pipe flows, the flow is inhomogeneous in the streamwise direction in spatially evolving boundary layers. The inflow is prescribed using the so-called recycle–rescale method proposed by Lund *et al.* (1998), where the flow field at a streamwise location downstream is rescaled as per known well-established theoretical

boundary layer scaling laws and reintroduced at the inflow. This way, the simulation generates its own inflow, described briefly as follows.

The velocities at the inflow plane, $x = x_{in}$, are written as

$$
\begin{aligned}
u(y, z, t) = \beta[&\gamma \bar{U}(x_r, y_r^o, t) + (1 - \gamma)U_\infty \\
&+ \gamma u'(x_r, y_r^o, z_r, t)] \\
&+ (1 - \beta)[\gamma \bar{U}(x_r, y_r^i, t) \\
&+ \gamma u'(x_r, y_r^i, z_r, t)],
\end{aligned}
\tag{A1}
$$

$$
\begin{aligned}
v(y, z, t) = \beta[&\bar{V}(x_r, y_r^o, t) + \gamma v'(x_r, y_r^o, z, t)] \\
&+ (1 - \beta)[\bar{V}(x_r, y_r^i, t) \\
&+ \gamma v'(x_r, y_r^i, z, t)],
\end{aligned}
\tag{A2}
$$

$$
\begin{aligned}
w(y, z, t) = \beta\gamma w'(&x_r, y_r^o, z, t) \\
&+ (1 - \beta)\gamma w'(x_r, y_r^i, z, t),
\end{aligned}
\tag{A3}
$$

where the $(\bar{\cdot})$ is the spanwise average through time, 'r' denotes the recycle plane, 'i' denotes the inner scale, 'o' denotes the outer scale. The inner scales are based on the $y^+ = y u_\tau / \nu$ scaling and the outer scales are based on $\eta = y/\delta_{99}$. Here β is Lund's weighting function as given in (A4), which is used to blend the inner and outer scales. The values of constants are $a = 4$ and $b = 0.2$ in the following:

$$
\beta(\eta) = \frac{1}{2} \left[\frac{1 + \tanh\left(\dfrac{a(\eta - b)}{(1 - 2b)\eta + b} \right)}{\tanh(a)} \right].
\tag{A4}
$$

The mean velocity profile is obtained by spanwise averaging at every time step and then averaging over a sliding time window. The averaging time window is initially set to $T = A\delta_{99,i}|_0/U_\infty$ where $A = 10$ to discard the transients and then switched to 100 once the transients die out. The running average,

$$
\mathcal{F}(t) = \left(1 - \frac{\Delta t}{T}\right) \mathcal{F}(t - \Delta t) + \frac{\Delta t}{T} f(t),
\tag{A5}
$$

where f is the instantaneous spanwise average. Finally, the averaging is switched to a simple running average with $T = T_0 + t - t_0$ where, t is the time in the simulation, t_0 is the time at which the running averaging was initiated and T_0 is the value of the averaging interval used prior to t_0. This mean boundary layer velocity profile is used to evaluate the scaling parameters $(\theta, \delta_{99}, u_\tau)$ as a function of the streamwise location.

In order to generate the desired turbulent inflow, the inflow parameters $u_{\tau,i}$, θ_i and $\delta_{99,i}$ are specified. The value of θ_i is kept fixed whereas $u_{\tau,i}$ is computed at every time step using the following, knowing the values of flow parameters at the recycling plane:

$$
u_{\tau,i} = u_{\tau,r} \left(\frac{\theta_r}{\theta_i}\right)^{(1/8)}.
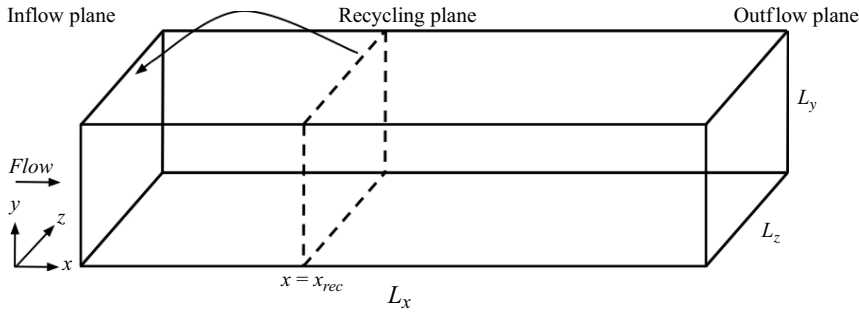\tag{A6}
$$

Figure 20. A schematic of the computational domain showing the recycle–rescale method. The velocities at recycling plane ($x = x_{rec}$) are rescaled and prescribed to the inflow plane at each time step to generate turbulent inflow (Lund *et al.* 1998).

The rescale parameter γ is defined as

$$\gamma = \frac{u_{\tau,i}}{u_{\tau,r}} = \left(\frac{\theta_r}{\theta_i}\right)^{(1/8)}, \tag{A7}$$

which is used to construct velocities at the inflow plane. The constructed inflow plane velocity profiles are adjusted through a Newton–Raphson scheme to obtain $\delta_{99,i}$.

A.2. *Validation*

Simulations are performed for spatially developing TBL for two inflow Reynolds number, $Re_{\theta,in} = 1410$ and 2200 using the numerical algorithm described in (2.1). The computational domain used for simulations is a box of length L_x, width L_z and height L_y as shown in figure 20. The subscripts x, y and z refer to streamwise, wall-normal and spanwise directions, respectively. Flow is from the left-hand side to the right-hand side. The wall is situated at $y = 0$ plane. No-slip boundary condition is applied on the wall. Convective boundary conditions are prescribed at the outflow. The boundary conditions on the top surface ($y = L_y$) are

$$\frac{\partial u}{\partial y} = 0, \quad v = U_\infty \frac{\partial \delta^*}{\partial x}, \quad \frac{\partial w}{\partial y} = 0, \tag{A8}$$

where δ^* is the boundary layer displacement thickness and U_∞ is the free stream velocity. At every time step, δ^* is computed from the mean velocity field as a function of x and then the derivative $\partial \delta^*/\partial x$ is computed as an average slope, whose value is usually small.

The θ_{in} is kept fixed at 0.1 for both cases. The location of recycling plane has to be sufficiently far away from the inflow and outflow to avoid any unphysical behaviour. The computational grid is uniform in streamwise (x) and spanwise (z) direction with a clustering near wall in wall-normal (y) direction to resolve fine near-wall flow structures. The details of the simulations are listed in table 4.

The profiles for mean velocity and second-order statistics from the low-*Re* case are compared with the DNS results at $Re_\theta = 1420$ (Schlatter & Örlü 2010), $Re_\theta = 1551$ and $Re_\theta = 1968$ (Jiménez *et al.* 2010) as shown in figure 21. The profiles are extracted at three streamwise locations for the low-*Re* case and two streamwise locations for the high-*Re* case (see table 4). The extracted profiles from the high-*Re* case are compared with DNS results at $Re_\theta = 2540$ and $Re_\theta = 3032$ (Schlatter & Örlü 2010) as shown in figure 22. The results from both cases show very good agreement with the DNS data available in the

Case	$Re_{\theta,in}$	L_x/θ_{in}	L_y/θ_{in}	L_z/θ_{in}	N_x	N_y	N_z	x_{rec}/L_x
Low-*Re*	1410	300	30	20	1000	200	200	27.5 %
High-*Re*	2200	300	30	20	1000	200	200	82.5 %

Table 4. Domain size and grid distribution for the DNS. Here, L_x, L_y and L_z are the domain size in the streamwise, wall-normal and spanwise directions, respectively; and N_x, N_y and N_z are the number of control volumes in those directions, respectively. Here x_{rec} is the location of the recycling plane and θ_{in} is the prescribed momentum thickness at the inflow. Here $Re_{\theta,in}$ is the prescribed inflow Reynolds number based on θ_{in}.
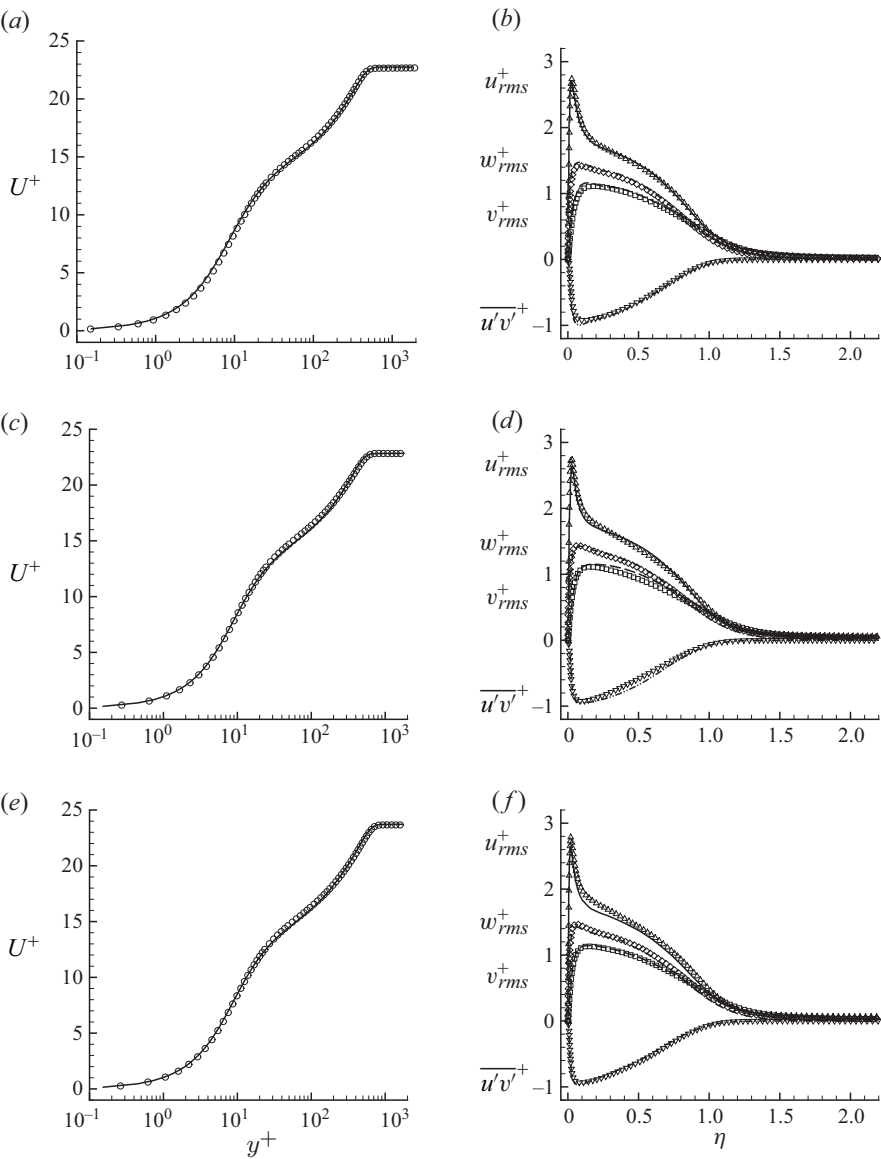

Figure 21. Low-Re: mean and second-order velocity statistics at $Re_\theta = 1420$ (*a*, *b*), 1551 (*c*, *d*) and 1968 (*e*, *f*). Symbols are DNS from Schlatter & Örlü (2010) (*a*, *b*) and Jiménez *et al.* (2010) (*c*−*f*).
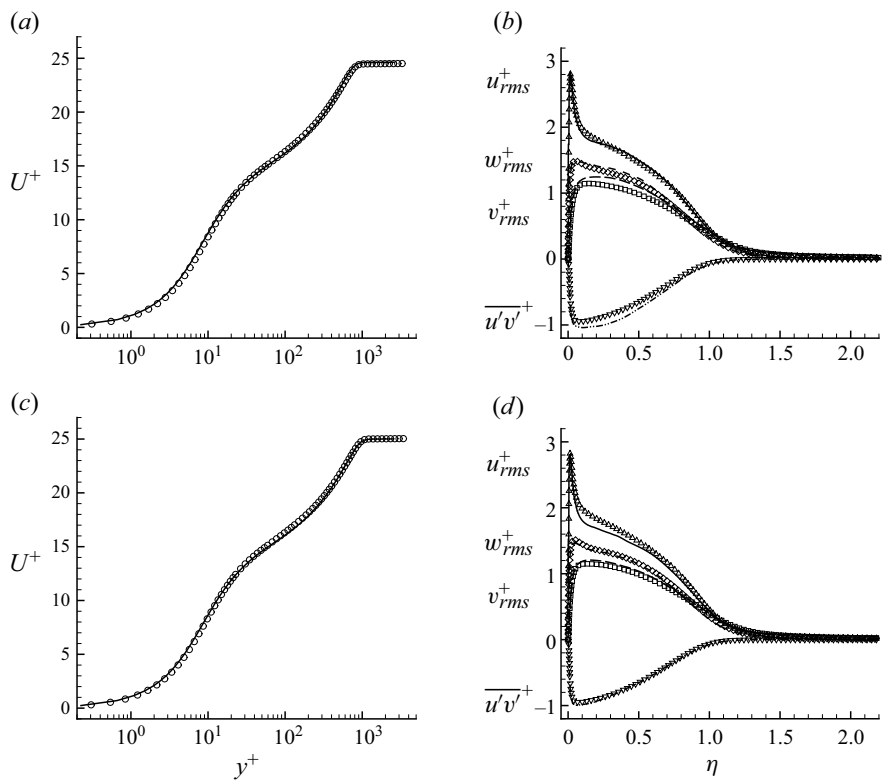
Figure 22. High-*Re*: mean and second-order velocity statistics at $Re_\theta = 2540$ (*a*, *b*) and 3032 (*c*, *d*). Symbols are DNS from Schlatter & Örlü (2010).

Case	x	Re_θ	x^+	y^+	z^+
Low-*Re*	0.255	1420	18.6	0.31	6.2
Low-*Re*	5.085	1551	18.5	0.31	6.17
Low-*Re*	20.985	1968	17.8	0.3	5.95
High-*Re*	8.925	2540	18.8	0.45	8.93
High-*Re*	21.765	3032	26.4	0.44	8.8

Table 5. Grid resolution at different streamwise locations in wall units. The streamwise (x) and spanwise (z) directions have uniform grid distribution whereas the grid is clustered near wall in wall-normal (y) direction. Here, y^+ is the first cell size near wall. The low-*Re* and high-*Re* are cases with $Re_{\theta,in} = 1410$ and 2200, respectively.

literature. The corresponding grid details are listed in table 5. Thus, the simulation method to generate a ZPG TBL of desired properties can be considered validated.

Appendix B. Sensitivity to domain size

Simulations were performed on two different computational domains, which differed only in the spanwise length (L_z). Domain 1 had $L_z = 3\delta_{99}$, where $\delta_{99} = 1$ is the boundary layer thickness at the inflow plane. Domain 2 had double the size in spanwise direction. Both
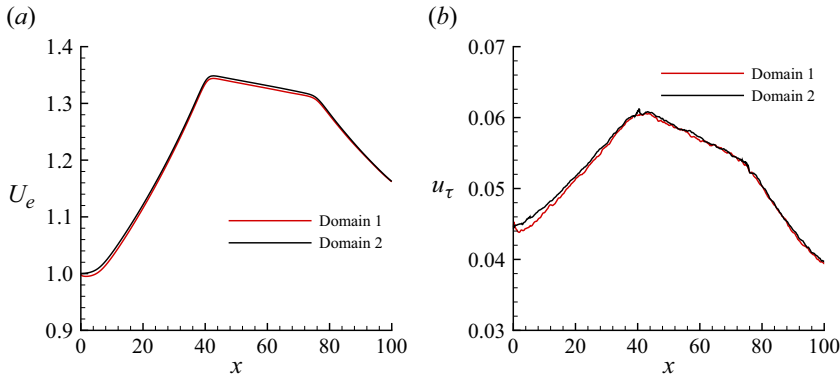
Figure 23. The streamwise variation of U_e (*a*) and u_τ (*b*) velocities are compared between Domain1 ($L_z = 3$) and Domain 2 ($L_z = 6$).
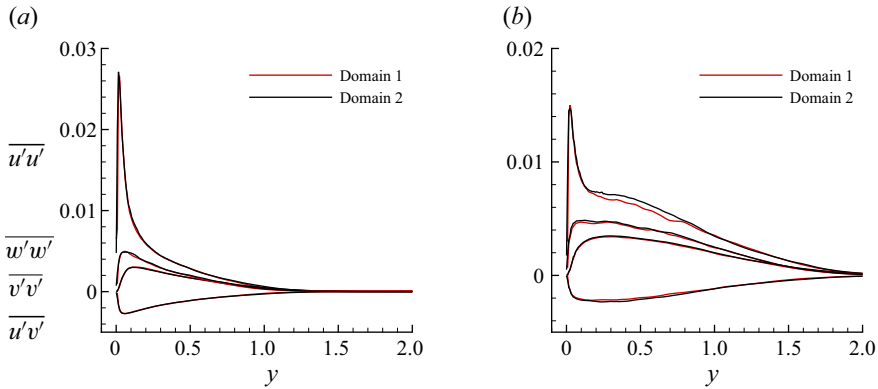

Figure 24. The wall-normal profiles of Reynolds stress components are compared between Domain1 ($L_z = 3$) and Domain 2 ($L_z = 6$) at Station 6 (*a*) and Station 12 (*b*).

computational domains had identical grid resolutions. Figure 23 shows the streamwise variation of U_e and u_τ for the two cases. Figure 24 shows the wall-normal profiles of Reynolds shear stress components at Stations 6 and 12 for the two cases. Note that the values are not normalised for direct comparison. Some difference can be observed at Station 12 in the streamwise Reynolds shear stress. The mean velocity profiles at these stations (not shown here) were identical for the two cases. Overall, the results suggest that Domain 2 was sufficiently wide for the present flow problem. Even wider domain is not expected to make any appreciable difference in the results shown in this work.

Appendix C. Additional profile comparisons

The profile comparisons with the reference data at Stations 2–5, 7, 8, 10 and 11 are shown for the mean velocity defect (figure 25), the r.m.s. of streamwise (figure 26) and wall-normal (figure 27) velocity fluctuations, and the Reynolds shear stress (figure 28). All the profiles are normalised by the local mean streamwise velocity in the free stream.
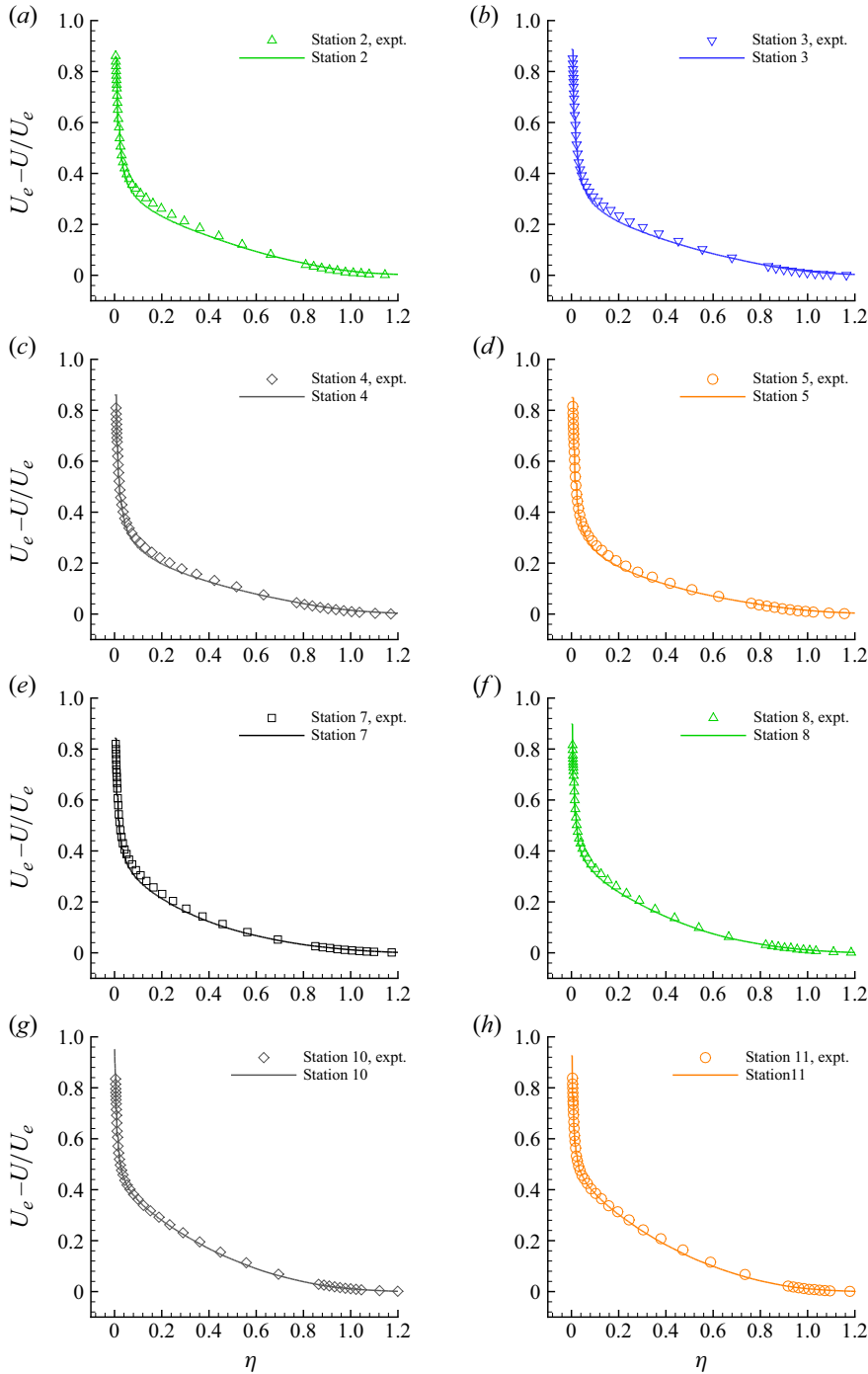
Figure 25. Mean velocity defect profiles (lines) are compared with the reference data (symbols) of Volino (2020a) at Stations 2–5 $(a-d)$, Stations 7–8 (e, f) and Stations 10–11 (g, h).
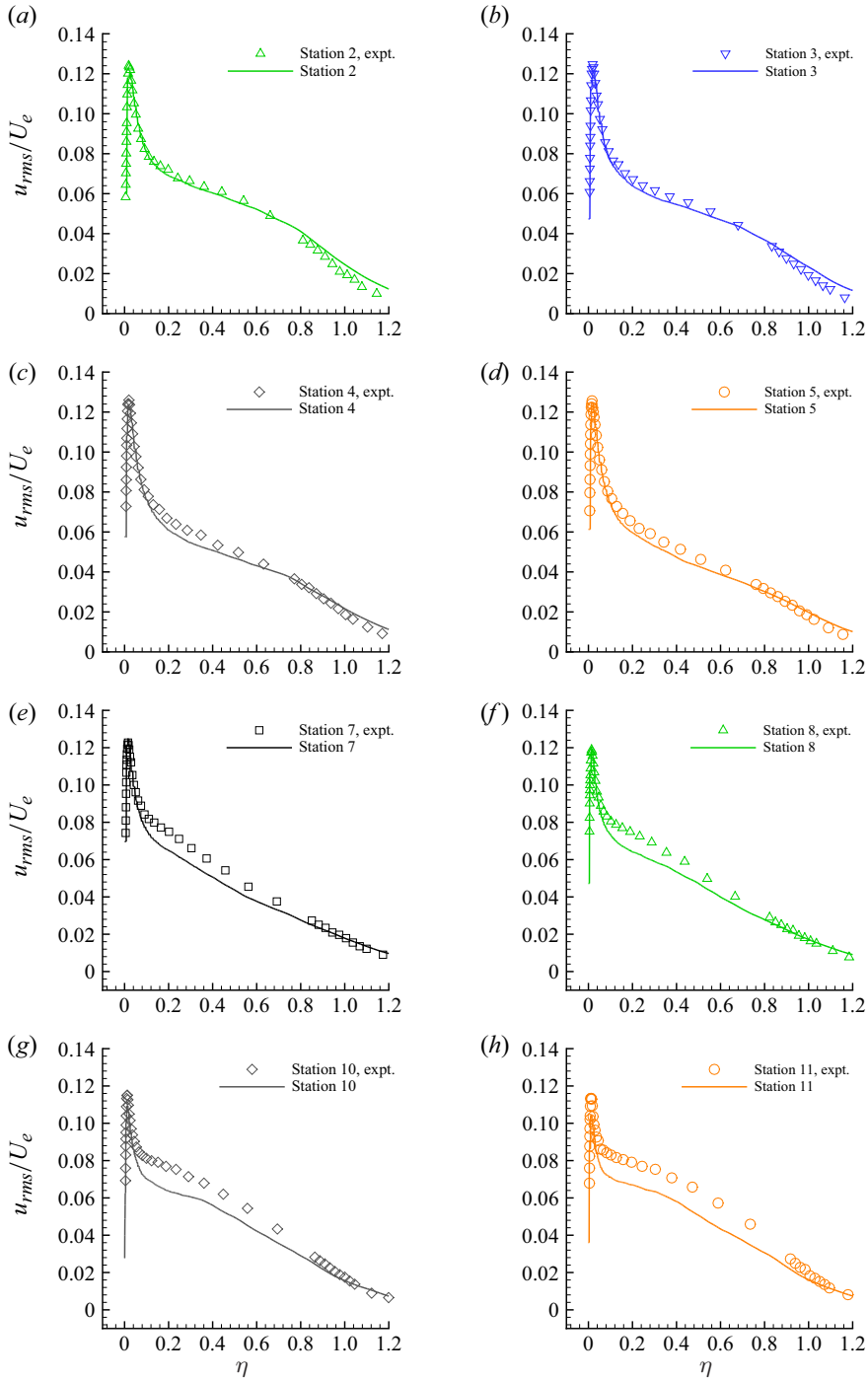
Figure 26. The r.m.s. of streamwise velocity fluctuations (lines) are compared with the reference data (symbols) of Volino (2020*a*) at the same stations as figure 25.
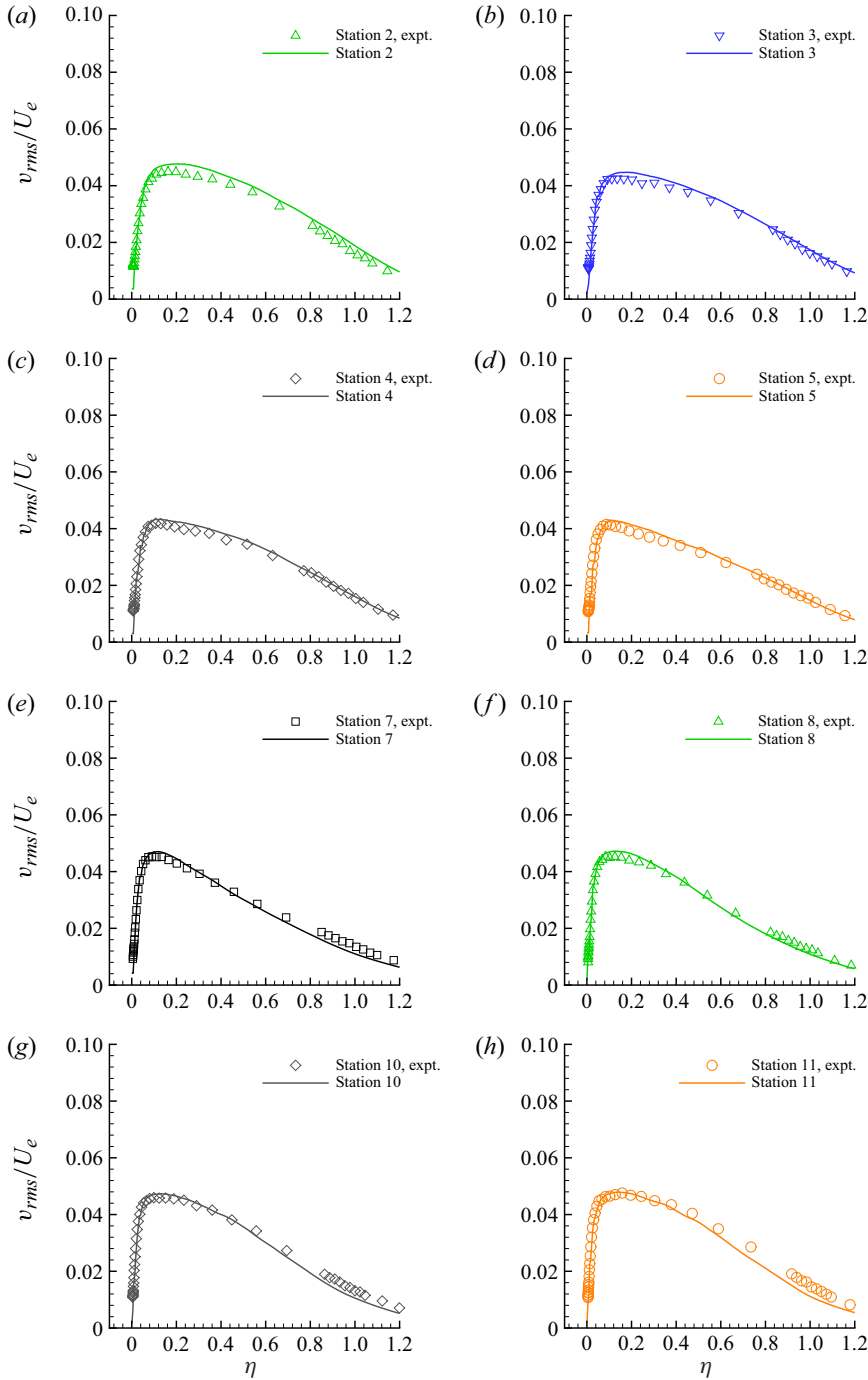
Figure 27. The r.m.s. of wall-normal velocity fluctuations (lines) are compared with the reference data (symbols) of Volino (2020*a*) at the same stations as figure 25.
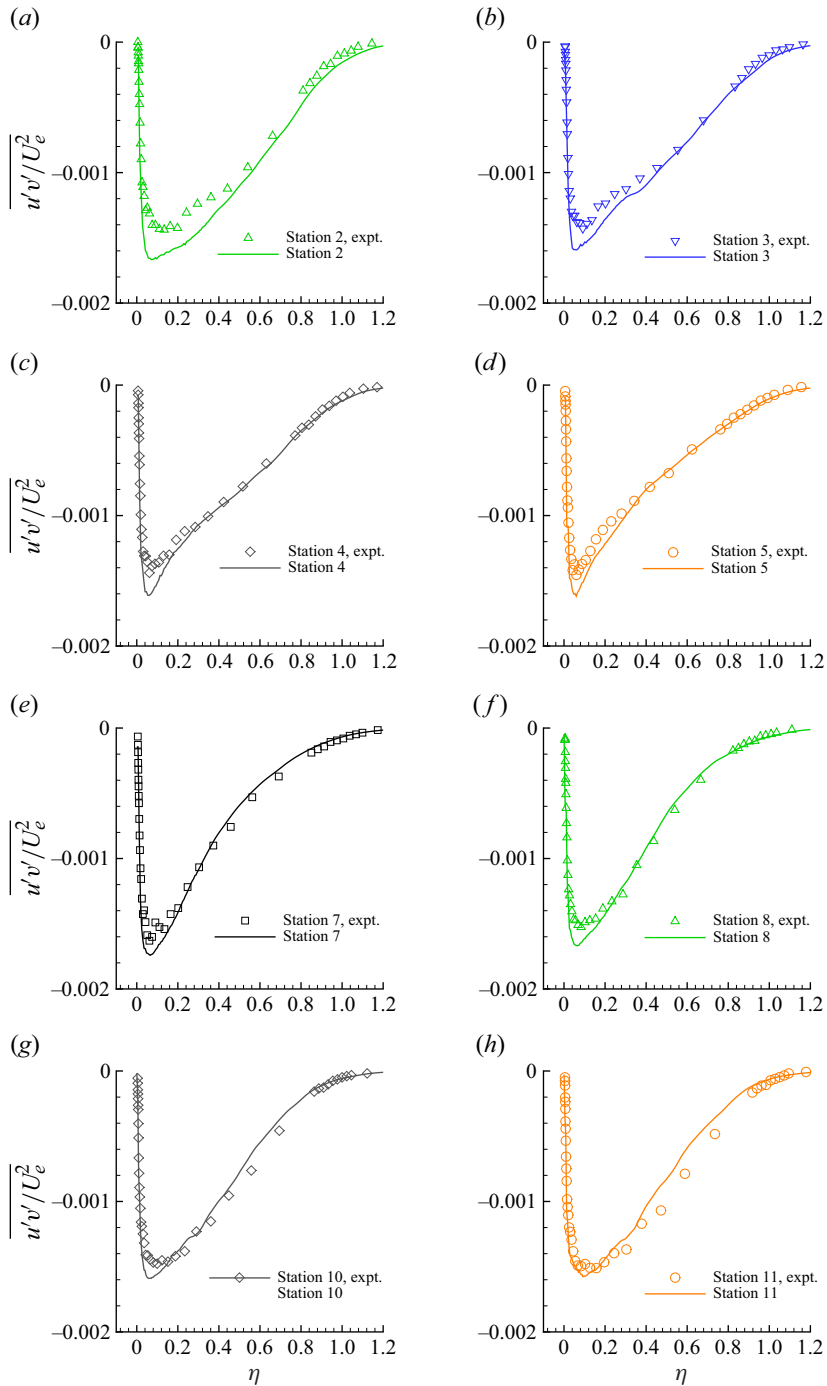
Figure 28. Reynolds shear stress profiles (lines) are compared with the reference data (symbols) of Volino (2020*a*) at the same stations as figure 25.

References

ALFREDSSON, P.H., ÖRLÜ, R. & SEGALINI, A. 2012 A new formulation for the streamwise turbulence intensity distribution in wall-bounded turbulent flows. *Eur. J. Mech. B/Fluids* **36**, 167–175.

ALFREDSSON, P.H., SEGALINI, A. & ÖRLÜ, R. 2011 A new scaling for the streamwise turbulence intensity in wall-bounded turbulent flows and what it tells us about the 'outer' peak. *Phys. Fluids* **23** (4), 041702.

ARAYA, G., CASTILLO, L. & HUSSAIN, F. 2015 The log behaviour of the Reynolds shear stress in accelerating turbulent boundary layers. *J. Fluid Mech.* **775**, 189–200.

AUBERTINE, C.D. & EATON, J.K. 2005 Turbulence development in a non-equilibrium turbulent boundary layer with mild adverse pressure gradient. *J. Fluid Mech.* **532**, 345–364.

BOBKE, A., VINUESA, R., ÖRLÜ, R. & SCHLATTER, P. 2017 History effects and near equilibrium in adverse-pressure-gradient turbulent boundary layers. *J. Fluid Mech.* **820**, 667–692.

CASTILLO, L. & GEORGE, W.K. 2001 Similarity analysis for turbulent boundary layer with pressure gradient: outer flow. *AIAA J.* **39** (1), 41–47.

DEVENPORT, W.J. & LOWE, K.T. 2022 Equilibrium and non-equilibrium turbulent boundary layers. *Prog. Aerosp. Sci.* **131**, 100807.

DRÓŻDŻ, A., ELSNER, W. & DROBNIAK, S. 2015 Scaling of streamwise Reynolds stress for turbulent boundary layers with pressure gradient. *Eur. J. Mech. B/ Fluids* **49**, 137–145.

FERNHOLZ, H.H. & FINLEY, P.J. 1996 The incompressible zero-pressure-gradient turbulent boundary layer: an assessment of the data. *Prog. Aerosp. Sci.* **32** (4), 245–311.

FERNHOLZ, H.H. & WARNACK, D. 1998 The effects of a favourable pressure gradient and of the Reynolds number on an incompressible axisymmetric turbulent boundary layer. Part 1. The turbulent boundary layer. *J. Fluid Mech.* **359**, 329–356.

GEORGE, W.K. 2006 Recent advancements toward the understanding of turbulent boundary layers. *AIAA J.* **44** (11), 2435–2449.

GERMANO, M., PIOMELLI, U., MOIN, P. & CABOT, W.H. 1991 A dynamic subgrid–scale Eddy viscosity model. *Phys. Fluids A* **3** (7), 1760–1765.

HARUN, Z., MONTY, J.P., MATHIS, R. & MARUSIC, I. 2013 Pressure gradient effects on the large-scale structure of turbulent boundary layers. *J. Fluid Mech.* **715**, 477–498.

JIMÉNEZ, J., HOYAS, S., SIMENS, M.P. & MIZUNO, Y. 2010 Turbulent boundary layers and channels at moderate Reynolds numbers. *J. Fluid Mech.* **657**, 335–360.

JONES, M.B., MARUSIC, I. & PERRY, A.E. 2001 Evolution and structure of sink-flow turbulent boundary layers. *J. Fluid Mech.* **428**, 1–27.

JONES, W.P. & LAUNDER, B.E. 1972 Some properties of sink-flow turbulent boundary layers. *J. Fluid Mech.* **56** (2), 337–351.

KITSIOS, V., SEKIMOTO, A., ATKINSON, C., SILLERO, J.A., BORRELL, G., GUNGOR, A.G., JIMÉNEZ, J. & SORIA, J. 2017 Direct numerical simulation of a self-similar adverse pressure gradient turbulent boundary layer at the verge of separation. *J. Fluid Mech.* **829**, 392–419.

KLEWICKI, J.C. 2010 Reynolds number dependence, scaling, and dynamics of turbulent boundary layers. *J. Fluids Engng* **132** (9), 094001.

KNOPP, T., REUTHER, N., NOVARA, M., SCHANZ, D., SCHÜLEIN, E., SCHRÖDER, A. & KÄHLER, C.J. 2021 Experimental analysis of the log law at adverse pressure gradient. *J. Fluid Mech.* **918**, A17.

KUMAR, P. & MAHESH, K. 2018 Large eddy simulation of flow over an axisymmetric body of revolution. *J. Fluid Mech.* **853**, 537–563.

KUMAR, P. & MAHESH, K. 2021 Simple model for mean stress in turbulent boundary layers. *Phys. Rev. Fluids* **6** (2), 024603.

KUMAR, P. & MAHESH, K. 2022 A method to determine wall shear stress from mean profiles in turbulent boundary layers. *Exp. Fluids* **63** (1), 6.

LAUNDER, B.E. & JONES, W.P. 1969 Sink flow turbulent boundary layers. *J. Fluid Mech.* **38** (4), 817–831.

LEE, J.-H. 2017 Large-scale motions in turbulent boundary layers subjected to adverse pressure gradients. *J. Fluid Mech.* **810**, 323–361.

LEE, J.-H. & SUNG, H.J. 2009 Structures in turbulent boundary layers subjected to adverse pressure gradients. *J. Fluid Mech.* **639**, 101–131.

LILLY, D.K. 1992 A proposed modification of the Germano subgrid-scale closure method. *Phys. Fluids A* **4** (3), 633–635.

LUND, T.S., WU, X. & SQUIRES, K.D. 1998 Generation of turbulent inflow data for spatially-developing boundary layer simulations. *J. Comput. Phys.* **140** (2), 233–258.

MACIEL, Y., WEI, T., GUNGOR, A.G. & SIMENS, M.P. 2018 Outer scales and parameters of adverse-pressure-gradient turbulent boundary layers. *J. Fluid Mech.* **844**, 5–35.

MAHESH, K., CONSTANTINESCU, G. & MOIN, P. 2004 A numerical method for large–eddy simulation in complex geometries. *J. Comput. Phys.* **197** (1), 215–240.

MARUSIC, I., MCKEON, B.J., MONKEWITZ, P.A., NAGIB, H.M., SMITS, A.J. & SREENIVASAN, K.R. 2010 Wall-bounded turbulent flows at high Reynolds numbers: recent advances and key issues. *Phys. Fluids* **22** (6), 065103.

MELLOR, G.L. & GIBSON, D.M. 1966 Equilibrium turbulent boundary layers. *J. Fluid Mech.* **24** (2), 225–253.

NARASIMHA, R. & SREENIVASAN, K.R. 1973 Relaminarization in highly accelerated turbulent boundary layers. *J. Fluid Mech.* **61** (3), 417–447.

PARK, N. & MAHESH, K. 2009 Reduction of the Germano-identity error in the dynamic Smagorinsky model. *Phys. Fluids* **21** (6), 065106.

PIOMELLI, U., BALARAS, E. & PASCARELLI, A. 2000 Turbulent structures in accelerating boundary layers. *J. Turbul.* **1** (1), 001.

PIROZZOLI, S. & SMITS, A.J. 2023 Outer-layer universality of the mean velocity profile in turbulent wall-bounded flows. *Phys. Rev Fluids* **8** (6), 064607.

POZUELO, R., LI, Q., SCHLATTER, P. & VINUESA, R. 2022 An adverse-pressure-gradient turbulent boundary layer with nearly constant. *J. Fluid Mech.* **939**, A34.

PRANDTL, L. 1904 Über flussigkeitsbewegung bei sehr kleiner reibung. In *Verhandl*, vol. III, pp. 484–491, Internat. Math.-Kong.

ROMERO, S., ZIMMERMAN, S., PHILIP, J., WHITE, C. & KLEWICKI, J. 2022 Properties of the inertial sublayer in adverse pressure-gradient turbulent boundary layers. *J. Fluid Mech.* **937**, A30.

SCHLATTER, P. & ÖRLÜ, R. 2010 Assessment of direct numerical simulation data of turbulent boundary layers. *J. Fluid Mech.* **659**, 116–126.

SIMPSON, R.L. 1989 Turbulent boundary-layer separation. *Annu. Rev. Fluid Mech.* **21** (1), 205–232.

SKOTE, M., HENNINGSON, D.S. & HENKES, R.A.W.M. 1998 Direct numerical simulation of self-similar turbulent boundary layers in adverse pressure gradients. *Flow Turbul. Combust.* **60** (1), 47–85.

SKÅRE, P.E. & KROGSTAD, P. 1994 A turbulent equilibrium boundary layer near separation. *J. Fluid Mech.* **272**, 319–348.

SMITS, A.J., MCKEON, B.J. & MARUSIC, I. 2011 High-Reynolds number wall turbulence. *Annu. Rev. Fluid Mech.* **43** (1), 353–375.

SPALART, P.R. 1986 Numerical study of sink-flow boundary layers. *J. Fluid Mech.* **172**, 307–328.

TOWNSEND, A.A. 1956 *The Structure of Turbulent Shear Flow*. Cambridge University Press.

VERMA, A. & MAHESH, K. 2012 A Lagrangian subgrid-scale model with dynamic estimation of Lagrangian time scale for large eddy simulation of complex flows. *Phys. Fluids* **24** (8), 085101.

VOLINO, R.J. 2020*a* Non-equilibrium development in turbulent boundary layers with changing pressure gradients. *J. Fluid Mech.* **897**, A2.

VOLINO, R.J. 2020*b* Reynolds number dependence of zero pressure gradient turbulent boundary layers including third-order moments and spatial correlations. *J. Fluids Engng* **142** (5), 051303.

WARNACK, D. & FERNHOLZ, H.H. 1998 The effects of a favourable pressure gradient and of the reynolds number on an incompressible axisymmetric turbulent boundary layer. Part 2. the boundary layer with relaminarization. *J. Fluid Mech.* **359**, 357–381.

WEI, T. & MACIEL, Y. 2018 Derivation of Zagarola-Smits scaling in zero-pressure-gradient turbulent boundary layers. *Phys. Rev. Fluids* **3** (1), 012601.

WU, W. & PIOMELLI, U. 2018 Effects of surface roughness on a separating turbulent boundary layer. *J. Fluid Mech.* **841**, 552–580.

YUAN, J. & PIOMELLI, U. 2014 Estimation and prediction of the roughness function on realistic surfaces. *J. Turbul.* **15** (6), 350–365.

YUAN, J. & PIOMELLI, U. 2015 Numerical simulation of a spatially developing accelerating boundary layer over roughness. *J. Fluid Mech.* **780**, 192–214.

ZAGAROLA, M.V. & SMITS, A.J. 1998*a* Mean-flow scaling of turbulent pipe flow. *J. Fluid Mech.* **373**, 33–79.

ZAGAROLA, M.V. & SMITS, A.J. 1998*b* A new mean velocity scaling for turbulent boundary layers. In *Proceedings of FEDSM'98*. ASME.